This is a preprint of an article that been submitted to Communications Earth & Environment and revised based on one round of peer review at that journal, but has yet to be formally accepted for publication.

Soil pore water evaporation and temperature influences on clay mineral paleothermometry

Daniel E. Ibarra[1,2] and Jaivime Evaristo[3]

1. Institute at Brown for Environment and Society, Brown University, Providence, RI, 02906 USA
2. Department of Earth, Environmental and Planetary Science, Brown University, Providence, RI, 02906 USA
3. Copernicus Institute of Sustainable Development, Utrecht University, Utrecht, The Netherlands

Corresponding author: Daniel E. Ibarra; daniel_ibarra@brown.edu

Abstract

Clay mineral isotope paleothermometry is fundamental to understanding Earth's climate system and landscape evolution. Status quo methods, however, assume constant factors, such as temperature and water isotopic compositions, and ignore seasonality, soil water evaporation and depth dependent temperature changes. We propose first-order modifications to address these factors and test them in a modeling framework using published data from various settings. Our forward model reveals that neglecting evaporation and seasonal soil temperature variability may lead to significant underestimations of clay formation temperatures, especially in Mediterranean settings. Our inverse model indicates that high-latitude Eocene clay formation temperatures were ~8°C warmer than modern, while Eocene river sediments in the Sierra Nevada show evaporation-influenced trends, suggesting that previous paleoelevation estimates were underestimated. Our framework demonstrates that explicit consideration of soil pore water evaporation and temperature variability is necessary when interpreting clay mineral isotope data in the context of temperature, hydroclimate and elevation reconstructions.

Introduction

Stable oxygen and hydrogen isotope methods are valuable tools for understanding Earth's system processes, such as temperature fluctuations and changes in the water cycle[1–5]. These methods rely on the isotopic fractionation that occurs during phase changes in the water cycle[6–10] and the equilibrium precipitation of minerals from surface waters preserved in geologic records[11–13]. However, few geologic records capture both oxygen and hydrogen stable isotope ratios in the same phase. To address this issue, researchers developed fluorination and pyrolysis methods for measuring oxygen and hydrogen stable isotope ratios in clay minerals in the 1970s[14,15].

In the field of clay mineral thermometry, scientists have used clay minerals as single mineral thermometers or in combination with other mineral phases to study terrestrial paleoclimate and paleoaltimetry[16–34] assuming integration over soil formation timescales (10^3 to 10^6 yrs). Similar approaches have been applied to marine and lacustrine cherts[35–38], and iron oxides[39–41].

In the field of stable isotope hydrology, the global meteoric water line (GMWL $\delta^2H = 8x\delta^{18}O + 10$) serves as the starting point for understanding hydrological processes[3,5,6]. Recent studies have considered the role of evaporated soil waters in both field and modeling studies[42–46]. However, the impact of evaporated soil waters on clay mineral thermometry has not been extensively examined in a systematic fashion to sufficiently quantify potential uncertainties (cf. ref. 19). Conversely, the implications of the temperatures and isotopic compositions at which clays form within the framework of evaporated soil waters in hydrology and weathering studies remain underexplored. With improvements in analytical laboratory techniques and by integrating clay mineral thermometry with stable isotope hydrology, we can potentially develop innovative tools to better understand clay formation processes. This holds particular promise for interrogating modern weathering profiles where factors such as soil-regolith moisture, soil pore water stable isotopes, solute geochemistry, mineral saturation, soil gases and temperature are measured[47–51]. However, to our knowledge, no such combined approaches have been explored yet.

Here, we propose a cross-disciplinary approach between these two fields. We reevaluate key assumptions in both fields and suggest a refined methodology for interpreting clay mineral stable isotope datasets from past and present weathering profiles. While the knowledge of critical zone water stable isotope systematics[2,52,53] has long been recognized, it has not been effectively integrated into a coherent modeling framework until now.

In the following we begin by reviewing the common thermometry assumptions used when interpreting clay mineral $^{2}H/^{1}H$ and $^{18}O/^{16}O$ variations in modern and paleo-weathering profiles. Next, we apply existing theories that account for the following three factors as first-order modifications to the status quo method: 1) co-variations in the seasonality of temperature and the isotopic composition of meteoric waters along the local meteoric water line (LMWL); 2) the role of pore water evaporation trends away from the LMWL; and 3) the impact of seasonal soil temperature variations with depth. Our point of departure is that these factors are important for, and relatively well constrained in, describing broad patterns across modern weathering and paleo-weathering datasets. Finally, as an example of our approach we test our developed use cases within a modeling framework that calculates clay $\delta^{18}O$ and $\delta^{2}H$ using measured soil pore water $\delta^{18}O$ and $\delta^{2}H$ (forward model), and vice versa (inverse model).

What is the status quo?

Isotopic fractionation of oxygen and hydrogen during clay mineral precipitation is valuable for thermometry applications. What we collectively describe here as the *status quo* method is extensively documented in previous studies[14,19,21,27,54–56]. Importantly, due to vapor pressure differences of water isotopologues, the fractionation factor ($\alpha_{clay\text{-}water} = R_{clay}/R_{water}$) of hydrogen between clays and water is less than unity at Earth surface temperatures. This results in clay minerals being more depleted in $\delta^{2}H$ than the putative isotopic composition of their source waters. The fractionation factor for oxygen, however, is greater than unity, resulting in isotopically enriched clay mineral $\delta^{18}O$ (see ref. 54 for further discussion). Together, the result is that clay minerals in equilibrium with waters during weathering and soil formation fall below and to the right of waters from which they form in $\delta^{18}O$-$\delta^{2}H$ cross plots (Box 1).

The simplicity of the status quo method has enabled researchers to infer mineral formation temperatures, as depicted by the gray lines parallel to LMWL in Box 1. These inferred temperatures have subsequently been employed to back-calculate the putative isotopic compositions of the 'source water' – specifically, the meteoric water from which the clay mineral would have originated. As such, the location of an inferred source water on the LMWL, alternatively the GMWL, informs an interpretation regarding the elevation, temperature and paleoenvironment associated with mineral formation (Box 1). Clay minerals $\delta^{18}O$ and $\delta^{2}H$, therefore, have been used as geochemical proxies in paleoclimate and, most significantly, paleoaltimetry research.

Box 1: The temperature-dependence of hydrogen and oxygen fractionation between clays and water

Mineral thermometry equations require an assumption about the covariation of $\delta^{18}O$ and $\delta^{2}H$ in source waters. Historically, this covariation has been assumed to be consistent with the LMWL or GMWL[19,21,27,54,55]. This assumption creates a system with three equations and three unknowns. Solving this system uses previously determined, mineral-specific fractionation factors[12,54,57,58]. This results in characteristic monotonic relationships in the form of 1000lnα versus 1/T or $1/T^2$ at different temperatures (clay lines and temperatures, respectively, in the figure).

By using the GMWL as a key constraint, previous researchers established single-mineral thermometer relationships between temperature and measured $\delta^{18}O$ and δ^2H of clay minerals. For example, the empirically derived kaolinite fractionation factors determined by ref. 55 for oxygen is:

$$1000 \text{ x } \ln{}^{18}\alpha_{\text{kaol-water}} = 2.76\text{x}10^6 \text{ x } T^{-2} - 6.75 \quad (1)$$

and for hydrogen is:

$$1000 \text{ x } \ln{}^{2}\alpha_{\text{kaol-water}} = -2.2\text{x}10^6 \text{ x } T^{-2} - 7.7 \quad (2)$$

Combining these equations with the GWML ($\delta^2H = 8\text{x}\delta^{18}O + 10$) results in a single mineral thermometry equation as presented by ref. 21:

$$3.0350 \text{ x } 10^6 T^{-2} = \delta^{18}O_{\text{kaolinite}} - 0.1250\text{x}\delta^2H_{\text{kaolinite}} + 7.0375 \quad (3)$$

Ref. 54 presented an analogous relationship for smectite:

$$3.54 \text{ x } 10^6 T^{-2} = \delta^{18}O_{\text{smectite}} - 0.125\text{x}\delta^2H_{\text{smectite}} + 8.95 \quad (4)$$

In the case of kaolinite, solving for equations 1-3 results in an array of clay minerals that would have formed at different temperatures (clay lines and temperatures in the figure). The status quo method, however, assumes that clay minerals form from waters that covary along the GMWL, and the temperature calculated by equation 3 or 4 is interpreted to be the mean annual temperature of a given location. Thus, a given array of measured $\delta^{18}O$ and δ^2H of kaolinite would invariably correspond to a source water that plots on the GMWL. A source water that is enriched in the heavy isotopes (i.e., a more positive δ value) informs an interpretation that the mineral must have formed under characteristic climatological (e.g., high temperature, maritime, summer precipitation) and topographic (e.g., low elevation) conditions (red filled circle on GMWL). Similarly, a source water that is depleted in the heavy isotopes (i.e., more negative δ values) informs an interpretation that the mineral must have formed under characteristic climatological (e.g., low temperature, continental, winter precipitation) and topographic (e.g., high elevation) conditions (blue filled circle on GMWL).

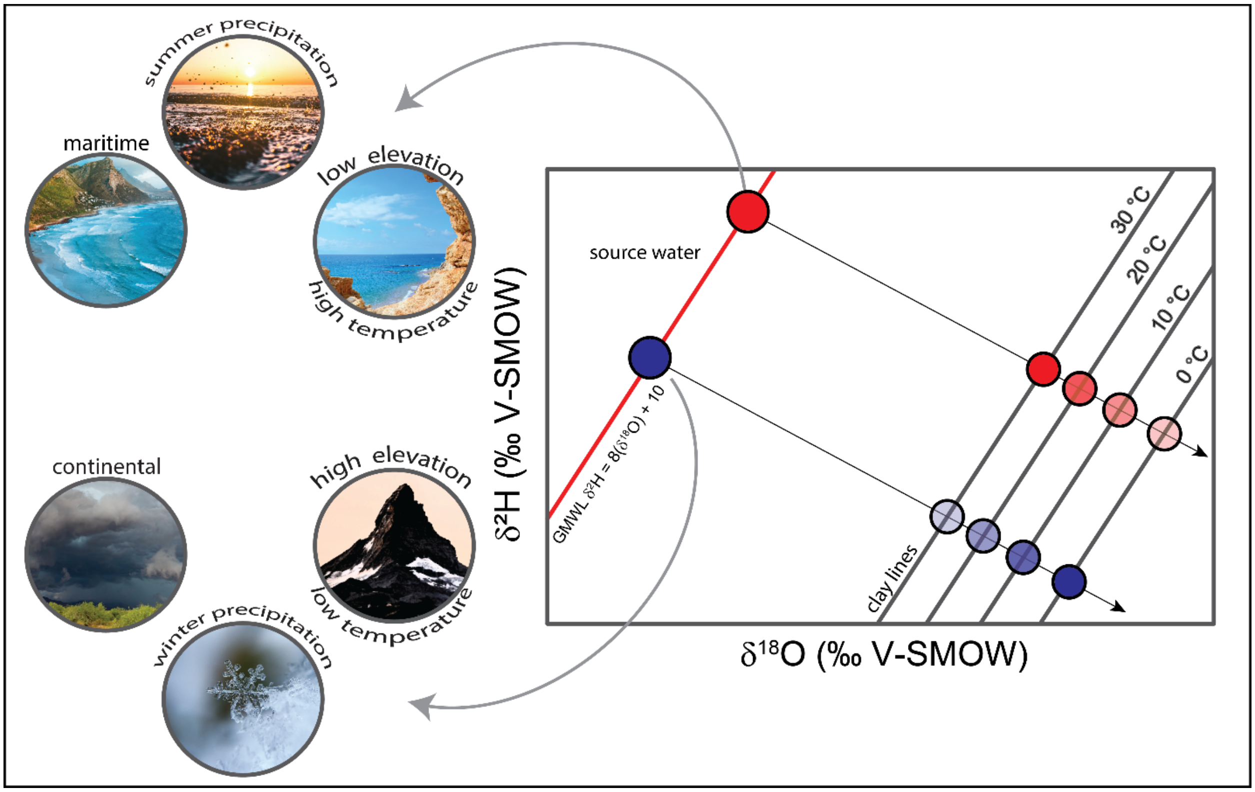

[Box 1 ends here]

What is wrong with the status quo?

Notwithstanding the simplicity of the status quo method, it invokes several key assumptions that may or may not be applicable in all settings. Firstly, the method assumes complete isotopic exchange of oxygen and hydrogen during weathering reactions. This assumption may only be plausible at high molar water/rock ratios[59,60] (other complications on the proxy fidelity of the method are detailed in the Supplemental Information). Secondly, the status quo method assumes that clay minerals form from waters that covary along the GMWL, or LMWL, and fractionate at the mean annual temperature of a given location. Previous studies, however, have shown that individual studies across different times and locations violate this assumption. That is, rather than clays (e.g., kaolinite and smectite) falling along slopes of ~8, many studies demonstrated δ^{18}O versus δ^{2}H arrays that were either steeper or shallower than expected[19,21,27,29–31]. Ref. 19 proposed a graphical framework for interpreting the effects of aridity and mean temperature changes. These effects, however, have not been formally tested within the framework of single-mineral clay thermometer calculations.

Further, previous work has not considered seasonal variability in the isotopic compositions of meteoric waters and temperature in greater detail. Thus, in the following we develop new use cases [essentially 'thought experiments'] exploring the impact of several confounding factors on clay δ^{18}O-δ^{2}H arrays. Our thought experiments, organized as cases in increasing complexity, take into account the following: Case 1) the role of seasonal co-variations of temperature and meteoric water isotopic composition; Case 2) the role of evaporatively enriched soil waters; and, Case 3) the role of seasonal soil temperature variability with depth. First, we present a qualitative description of each use case (Theory). Then, we present model implementations of the cases (Simulations). Finally, we implement the models using real-world datasets (Applications).

Case 1 Theory. The role of seasonal co-variations of temperature and meteoric water isotopic composition

The amount and isotopic composition of precipitation tend to fluctuate seasonally in a coherent fashion with temperature across the Earth's continents, showing both positive and negative covariations[5]. These variations generally result from shifting precipitation patterns based on latitude, such as the contrast between monsoonal and synoptic precipitation delivery[2,61,62].

For example, during tropical summers, $\delta^{18}O$ and $\delta^{2}H$ of precipitation decrease due to the 'amount effect' predominating monsoon rainfall[5]. Consequently, this can lead to a negative correlation between temperature and the $\delta^{18}O$ and $\delta^{2}H$ values of precipitation. On the other hand, in mid-to-high latitudes, changes in moisture source, humidity and precipitation temperature typically lead to a positive correlation between temperature and $\delta^{18}O$ and $\delta^{2}H$ values of precipitation, with the most depleted values recorded during winter. In Mediterranean climates on the western side of major continents, winters often coincide with the wet season.

In the subsequent simulations detailed below, we focus on the influence of seasonal positive and negative correlations between air temperature and the isotopic composition of precipitation. This focus is specific to the single-mineral clay thermometers presented in equations 1 and 2 (cf. ref. 55).

Case 1 Simulations

Figure 1 shows the simulation results from our model conceptualization (Case 1), which accounts for the seasonality of precipitation isotopic composition and temperature at which the clay, in this instance kaolinite, forms. Case 1 presents some modifications to the status quo method concerning kaolinite lines that were used widely in previous works[19,21,27,30,55].

Initially, we examine a scenario where the waters forming the clay fall along a defined meteoric water line (in this case, the GMWL), with no evaporation (depicted by open black circles in Figure 1A). Variations parallel to clay lines of constant temperature solely arise from seasonal shifts in meteoric waters (black circles in Figure 1B). Long-term shifts in the annual average isotopic composition of precipitation, assuming constant temperature as outlined by ref. 19, would align with arrays parallel to clay lines (Box 1). These shifts could be due to changes in elevation over long, 10^{6}-yr tectonic timescales or in atmospheric circulation over both long and short timescales. However, when considering these isotopic composition changes due to elevation over tectonic timescales, it is important to note that they are likely to be accompanied by changes in temperature[63] as well.

We proceed by incorporating both positive and negative covariation in the seasonal isotopic composition of precipitation and temperature (green and orange points in Figure 1B; also see inset for illustration). Temperature plays a role in equilibrium condensation fractionation processes during precipitation, which leads to positive correlations, especially in mid-latitude regions such as Mediterranean climates[64]. Upon implementing this seasonal, i.e., monthly, calculations, a rotation is evident around the mean annual temperature line. This yields a steeper seasonal clay line than the status quo clay lines, with a slope close to 12.1 (green points). In contrast, when there is a negative correlation between the isotopic composition of precipitation and temperature – less frequent but observed in high elevation, monsoon-dominated regions – the rotation manifests with a shallower slope, around 5.9 (orange points). Importantly, these values, 12.1 and 5.9, are only indicative for the example scenarios we have chosen. The actual rotational slope depends on the degree of seasonality in the isotopic composition of precipitation and temperature. In the following section, we will modify this approach by incorporating depth-dependent trends in soil pore water stable isotopes and temperature fluctuations.

We note, however, some important caveats associated with Case 1. We posit that the soil water from which the clays form exhibits negligible residence time. It is also assumed that the isotopic composition of the soil pore water undergoes a complete reset with each seasonal cycle. Future use cases may consider to resolve these assumptions.

Case 2 Theory: The role of evaporatively enriched soil waters and seasonal temperature variations with depth

When precipitation water infiltrates the soil, some may evaporate. This leads to an enrichment of heavy isotopes in the remaining soil water due to both equilibrium and kinetic fractionation, which refers to the preferential transport of lighter water isotopologues during evaporation – in decreasing order of preference: $H_2{}^{16}O$ > $HD^{16}O$ > $H_2{}^{18}O$. Consequently, due to the kinetic fractionation component the correlation between $\delta^{18}O$ and δ^2H for water undergoing evaporation deviates from the GMWL. As defined by ref. 62, this divergence is termed as deuterium excess (*d*-excess = $\delta^2H - 8x\delta^{18}O$). It means that the lesser the *d*-excess value, the stronger the evaporation effect on a water sample.

A meta-analysis of 65 peer-reviewed papers between 1990 and 2017 demonstrated an increasing trend in the median *d*-excess of soil waters with soil depth across climate types[42]. This suggests that soil waters close to the surface tend to experience more evaporation and greater fractionation than those at deeper layers[65]. Further, in a $\delta^{18}O$-δ^2H cross plot, it was predicted[66] that global range of soil water evaporation slopes lies between 2 and 3. This range is notably less steep compared to the 4-5 range for lakes[66], consistent with the available data at the time. The 2-3 range also aligns with the 3.1-3.4 range indicated in a later modeling study[45].

In this study, our focus is on understanding the impact of modern evaporated soil waters on clay mineral thermometry. We specifically focus on soil evaporation slopes between 2 and 3 for each modern evaporated soil water, so as not to assume that all evaporated soil water samples originate from a single source[44]. This enables us to determine the isotopic composition during clay formation for a given modern evaporated soil water sample rather than running a trendline through all modern evaporated soil water samples that intersect with the LMWL.

To simulate soil pore water evaporation, we apply the model of steady-state evaporation and diffusion as proposed by ref. 53, following the approach of ref. 67. who used it to model soil carbonate $\delta^{18}O$ in semi-arid regions. The model shows an asymptotic relationship with depth (z_i) between the amount weighted average precipitation value ($\delta^{18}O_{precipation}$) and a surface soil water value ($\delta^{18}O_{surface}$). This value is defined by an assumed soil evaporation slope and seasonal fluctuations of precipitation $\delta^{18}O$ and δ^2H[53] (shown here for $\delta^{18}O$):

$$\delta^{18}O_i = (\delta^{18}O_{surface} - \delta^{18}O_{precipitation}) \text{ x } (\exp(-z_i/z^*)) + \delta^{18}O_{precipitation} \qquad (5).$$

The upward movement of water as the soil dries causes a decrease in $\delta^{18}O$ and $\delta^{2}H$ with depth *i*. This decrease is linked to a characteristic decay length (z*) determined by the evaporation rate, effective diffusivity, tortuosity and porosity of a soil profile[53,67–69]. In the upcoming calculations, we will apply equation 5 monthly to our hypothetical pore water arrays, assuming an evaporation slope of 3 and accounting for seasonal variations in precipitation $\delta^{18}O$ and $\delta^{2}H$. Subsequently, we will solve equation 5 for wet and dry seasons in our data-model comparison using modern field measurements of soil pore water $\delta^{18}O$ and $\delta^{2}H$ in a Mediterranean climate setting.

In addition to the complexities imposed by depth trends in pore water $\delta^{18}O$ and $\delta^{2}H$ composition, it is important to consider that the isotopic composition of authigenic soil minerals (i.e., minerals that form *in situ* within the soil environment) records the soil temperature at the moment those minerals precipitate, rather than the instantaneous or annual average air temperature.

An analogous example is found in recent studies centered on carbonate clumped isotope signatures (Δ_{47}) of soil carbonates. These studies have identified potential biases in soil carbonate formation temperatures: soil temperatures recorded by carbonates may be warmer than annual or seasonal air temperatures due to radiative heating effects, or colder due to seasonal biases[70–73]. In this modeling work we do not explicitly include radiative heating effects, but do include seasonal biases due to dampened temperature fluctuations with depth (see below). Nevertheless, clay mineral formation in weathering profiles and soils are likely less seasonally biased than carbonates, an assumption made by some recent modeling efforts[74]. While formation may be less punctuated for clays than carbonates, the *amount* of clay produced seasonally may fluctuated due to moisture content, soil water acidity and transient changes in infiltration rate. This fact has been harnessed when both are measured together within the same profile and/or stratigraphic sections and time intervals[22,23,26]. That said, future work on modern weathering profiles, using the framework presented here, may help better assess temperature biases for carbonate clumped isotopes and soil clay stable isotopes.

Seasonal (and daily) air temperature variability is dampened and delayed with depth in the soil column, according to a heat diffusion equation at a given depth (z) and time (t)[52]:

$$T_{z,t} = T_{avg} + A_o[\sin(\omega t - z/d)]/e^{z/d} \qquad (6),$$

where T_{avg} is the mean annual air temperature, A_o is the seasonal amplitude, ω is radial frequency (2π/year), and d is the damping depth. The damping depth is a function of the thermal conductivity and volumetric heat capacity of the soil[52,71].

Recently, ref. 69 estimated an average damping depth of 153 cm, using typical thermal conductivity and heat capacity values. In this work, we adhere to ref. 69's assumption of a damping depth of 153 cm. We apply equation 6 on a monthly basis for our hypothetical $\delta^{18}O$ and $\delta^{2}H$ clay arrays and seasonally for our data-model comparison in the subsequent theoretical and applied calculations.

Cases 2 Simulations

Except for inceptisols, clay minerals typically do not form near the surface of soil and weathering profiles, due to the depletion of primary minerals from which they form. Instead, clay mineral weathering fronts are often associated with weathering fronts at depths of tens to hundreds of centimeters, depending on climate, lithology and soil age[75–84]. However, processes like soil pore water evaporation and temperature fluctuations may influence the isotopic composition of clay minerals with depth near, at, and below the weathering front. In this work, we strive to model the expected depth profile of clay mineral isotopic composition accurately as a function of both processes. However, we do not suggest at what depths clay mineral formation is happening. That would require a depth-dependent reactive transport model[80].

Figure 1C illustrates the results of monthly soil evaporation trajectories. The maximum evaporative values along monthly evaporation slopes of 3 determine the $\delta^{18}O_{surface}$ and $\delta^{2}H_{surface}$ values in equation 5. This leads to an enrichment towards the surface in pore water values, as displayed in Figure 1D for $\delta^{18}O$. Additionally, temperature variation at the surface is set to co-vary positively with the $\delta^{18}O$ and $\delta^{2}H$ of precipitation (e.g., a mid-latitude type system), and is propagated downward as described by equation 6 and in Figure 1E. We note that the evaporation slope of 3, albeit within the 3.1-3.4 range modeled by ref. 44, neglects the possible effects of seasonal differences. Future use cases may consider to resolve this assumption because the extent of evaporation could vary seasonally as a function of temperature, relative humidity, and residual water fraction.

Because of the differences in fractionation factor magnitudes (kinetic evaporation slopes versus clay mineral formation temperatures), the monthly modeled $\delta^{18}O$ of kaolinite trends with depth intersect (Fig. 1F), whereas the less sensitive $\delta^{2}H$ system mainly represents a translation of the pore water depth trend (Fig. 1G).

Translating these calculations into monthly $\delta^{18}O_{kaolinite}$ versus $\delta^{2}H_{kaolinite}$ trajectories, compared to the status quo thermometry clay line contours (Fig. 1H), highlights several potential issues with the status quo methodology. Most significantly, the effect of substantial evaporation away from the GMWL results in widely variable trajectories, dependent on the relationship between the timing of soil pore water evaporation and the timing of clay mineral formation (Fig. 1H).

It is entirely possible that soil pore waters, which are evaporatively enriched, have sufficiently long residence times to carry out net weathering reactions forming clays in the soil profile[85]. Hence, these are the most likely to be recorded. Such trends have been robustly observed in the geologic record[21]. However, on the other hand, if pore water falling close to the meteoric water line are the dominant isotopic composition from which clays form, the influence of soil temperature variability in response to seasonal temperature fluctuations is non-linear. This results in monthly trajectories counter to (and in some cases perpendicular to) the status quo clay line thermometry contours. Such trends have also been observed previously in some Cenozoic clay isotope datasets[19,29].

Applications to real-world datasets

In the following section, we test the application of the Cases 1 and 2 models with data from modern and paleo soil water datasets. We refer to the models that underpin our data-model comparisons as forward and inverse models.

The *forward* model uses modern soil water $\delta^{18}O$ and $\delta^{2}H$ data ($\delta^{18}O_{sw}$ and $\delta^{2}H_{sw}$, respectively) as input to generate $\delta^{18}O$ and $\delta^{2}H$ values of kaolinite ($\delta^{18}O_{kaol}$ and $\delta^{2}H_{kaol}$, respectively) as output:

$$\delta^{18}O_{kaol} = \delta^{18}O_{sw} + 1000\ln^{18}\alpha_{kaol\text{-}water} \tag{7}$$

$$\delta^{2}H_{kaol} = \delta^{2}H_{sw} + 1000\ln^{2}\alpha_{kaol\text{-}water} \tag{8}$$

where the second terms in equations (7) and (8) are the same as in equations (1) and (2). We underline that these calculations, following ref. 57, assume that $1000\ln\alpha$ is the difference between the water and clay mineral composition, which is a commonly used approximation. The inaccuracy introduced by this approximation is comparatively minor, less than 2 °C, depending on the source water's initial composition and the clay formation temperature.

The *forward* model seeks to answer the question: Given $\delta^{18}O_{sw}$ and $\delta^{2}H_{sw}$ measurements, resulting from relatively well-constrained processes that lead to a sample plotting on or below the LMWL, how well can the calculated $\delta^{18}O_{kaol}$ and $\delta^{2}H_{kaol}$ agree or disagree either with the status quo method or any of the model conceptualizations (Cases 1-3)? We implement the forward model at two locations: one at a low-latitude site in Luquillo, Puerto Rico[86], and another at a mid-latitude site in Oregon[50].

The *inverse* model uses $\delta^{18}O_{kaol}$ and $\delta^{2}H_{kaol}$ data to predict the plausible values of $\delta^{18}O_{sw}$ and $\delta^{2}H_{sw}$ that best explain the observed kaolinite observations. The inverse model seeks to answer the question: Given $\delta^{18}O_{kaol}$ and $\delta^{2}H_{kaol}$ measurements, resulting from somewhat poorly-constrained processes, to what extent can the calculated $\delta^{18}O_{sw}$ and $\delta^{2}H_{sw}$ agree or disagree with the relatively well-constrained physics of covariations on or below the LMWL? We implement the inverse model using datasets from two studies: Eocene high latitude Finland[30], and another from the Eocene mid-latitudes in the western United States[21].

Forward model: Application to modern soil pore water datasets

Figure 2 shows results of the forward model, implemented at Luquillo, Puerto Rico (Fig. 2A and Fig. 2B) and Corvallis, Oregon (Fig. 2C and Fig. 2D). Average monthly precipitation $\delta^{18}O$ and air temperature are generally negatively correlated at Luquillo (Fig. 2B inset; Pearson's r -0.86, p-value=0.0004) and positively correlated at Corvallis (Fig. 2D inset; Pearson's r 0.89, p-value<0.0001).

At Luquillo, using modeled (equation 6) soil depth-dependent temperatures of between 25 and 26.6 °C as inputs to the forward model results in clay formation temperatures ranging from 12 to 30 °C (Fig. 2A and 2B). These estimates, however, cluster around 24 °C, close to the modern mean annual temperature of ~26 °C. The trendline slope of all kaolinite $\delta^{18}O$ and $\delta^{2}H$ (7.6 ±0.25 s.e.; dashed blue line Fig. 2B), which accounts for monthly air temperature and meteoric water isotopic compositions, is shallower than the slope of LMWL (9.4; Fig. 2A, solid red line). The shallower kaolinite trendline slope reflects the slight negative covariation between monthly precipitation isotopic compositions and air temperature (Fig. 2B inset). This suggests that, at this location where precipitation water $\delta^{18}O$ and air temperature are negatively correlated, purely atmospheric considerations (Case 1) should sufficiently describe kaolinite formation temperatures to first order. We interpret this as underlining the importance of precipitation water $\delta^{18}O$ and air temperature seasonal variability in estimating kaolinite formation temperatures. That said, sufficient data, ideally depth resolved, would be necessary to define the kaolinite trend as the most evaporatively enriched pore water data from Luquillo translate to temperatures <20 °C if taken at face value.

At Corvallis, using soil depth-dependent temperatures of between 8.4 and 16.4 °C as inputs to the forward model results in clay formation temperatures ranging from 0 to 20 °C (Fig. 2C and 2D). These estimates, however, cluster around 10 °C, close to the modern mean annual temperature of ~9 °C. The trendline slope of all kaolinite δ^{18}O and δ^{2}H (11 ±1.4 s.e.; dashed blue line Fig. 2D) is steeper than the slope of LMWL (5.9; Fig 2C, solid red line). The steeper kaolinite trendline slope reflects the positive covariation between monthly precipitation isotopic compositions and air temperature (Fig. 2D inset). The kaolinite trendline slope (Case 1), however, is considerably steeper than the dry season (6.1 ±0.18 s.e.; dashed green line Fig. 2D) and wet season (3.6 ±0.08 s.e.; dashed red line Fig. 2D) kaolinite slopes (Case 2) that account for seasonal soil temperature gradients and evaporative isotopic enrichment. This suggests that, at this location where precipitation water δ^{18}O and air temperature are positively correlated with a large seasonal amplitude, purely atmospheric considerations (Case 1) will tend to underestimate kaolinite formation temperatures. Atmospheric and soil evaporation considerations (Case 2) more closely approximate the plausible expectation that kaolinite formation temperatures of these soils are likely to be warmer than the case would be in a purely atmospheric case.

Patterns of kaolinite formation temperatures are also apparent with depth, suggesting a depth-dependent decrease in temperature. That is, evaporatively enriched soils close to the surface tend to correspond to warmer clay formation temperatures, systematically from 20 cm down. There is, however, an apparent departure of kaolinite values from Case 2 that accounts for purely soil evaporation (Fig. 2D, green and red dashed lines). This example demonstrates the importance of both soil temperature gradients, in addition to the role of precipitation water δ^{18}O and air temperature seasonal variability, in setting the isotopic composition of kaolinite and thus the inferred kaolinite formation temperatures. Additionally, it is clear from this example that pairing soil pore water and kaolinite stable isotope datasets with inferred weathering front advance depths[77,80] would provide insights into the timing (seasonality) and dominant depth(s) of clay mineral formation. As far as we are aware, no paired soil pore water and modern clay stable isotope exists in the published literature to allow benchmarking of our model.

Inverse model: Application to paleo weathering profile datasets

Next, to illustrate the concepts developed in this paper we turn to two geologic clay stable isotope datasets from the literature. We note that Holocene and Last Glacial Maximum soil kaolinite datasets from Colombia were previously published by ref. 17 but no accompanying soil pore water data is available. Both of the geologic datasets contain paired kaolinite hydrogen and oxygen isotope values, however, the trends relative to the GMWL are opposite, displaying steeper and shallower slopes (e.g., Fig, 1B).

In Figure 3A, we plot Eocene kaolinite data from ref. 30, derived from weathering profiles in Finland[87,88]. These data come from deep weathering zones, between 17 and 76 m, where we anticipate minimal influence of evaporation. (See however ref 89. Superimposing Case 1 shows a clay array with a slope of ~32 (Case 1a,dashed blue line Fig. 3A). The best-fit line to the measured kaolinite data has a slope of 5.7 (dashed black line Fig. 3A). Case 1 represents a parsimonious explanation for the orientation of the data, which is achieved by uniformly increasing the formation temperature by ~8 °C warmer than modern day air temperature. The inference of warmer temperatures was made by ref. 30, but the kaolinite array slope >8 was not described. Isotope-enabled global climate model simulations suggest that while a compressed (smaller range in $\delta^{18}O$ and $\delta^{2}H$) GMWL would have been present in the Eocene, the slope and intercept of the GMWL would have been similar to today[90]. As such, the counterclockwise rotation about the GMWL observed in the Finland kaolinites suggests: 1) no role for evaporation in a deep weathering zone, 2) positive covariation in the seasonality of temperature and precipitation $\delta^{18}O$-$\delta^{2}H$, and 3) formation temperature ~8 °C warmer than modern, though as we illustrate in the example from Corvallis above, interpreting such data with respect to paleotemperatures requires a systematic depth-dependent approach.

The second contrasting example is from weathered Eocene river sediments from the west flank of the northern Sierra Nevadas[21,91–94]. The $\delta^{2}H$ of the kaolinites were originally published by Mulch et al. (2006) to illustrate relatively high Eocene elevations, which were also confirmed by $\delta^{2}H$ analyses of volcanic glass and organic biomarkers[95,96]. Subsequently, ref. 21 paired the kaolinite $\delta^{2}H$ measurements on the same samples used by ref. 91 and found a shallower inferred $\delta^{18}O$ gradient and an apparent $\delta^{18}O$-$\delta^{2}H$ trend that reflected evaporation in the weathering zone with a slope of ~2.3 across the entire dataset (dashed black line, Fig. 3D). This finding is not surprising given that these Eocene river gravels represent immature, likely shallow, weathering profiles. However, waters along the windward side of a mountain range such as the Eocene Sierra Nevada should fall along a meteoric water line similar to today (slope of ~7.3)[89]. As such, in Figure 3D we apply our methodology here to explain how previous estimates by ref. 21 likely used source water values more enriched than the local meteoric values, resulting in a possible underestimate of past elevation. To do so requires assuming a warmer temperature of formation, ~33 °C (previously estimate of 23.2±6.4 °C[21]) and back calculating the pore water values along the inferred evaporation slope (~2.3). This assumes a summertime Eocene formation temperature and a strongly evaporative system (although actual sampling depths in the various weathering profiles were not quantified). Doing so places the most depleted samples near the modern local meteoric water line and calculation of source waters are presented in histograms in Figure 3. This set of calculations demonstrates that with some assumptions, such as warmer (likely summertime) formation temperatures during the Eocene hothouse and maximally evaporative soil pore water conditions, applying our inverse model approach better aligns the previously published clay $\delta^{18}O$-$\delta^{2}H$ stable isotope data with the volcanic glass and organic biomarker paleoelevation estimates (cf. ref. 97) of ~2.5 km with source water $\delta^{18}O$ compositions of -8 to -12‰ (Figure 3F).

Outlook and Conclusions

The framework developed here extends the utility of paired clay $\delta^{18}O$ and $\delta^{2}H$ datasets from geologic and modern weathering profiles. While the factors described here necessarily complicate the use of $\delta^{18}O$ and $\delta^{2}H$ measurements as a single mineral thermometer, our work outlines the approaches needed to develop a robust ‘proxy system model’[69,98–100]. We demonstrate how such measurements on modern weathering profiles, which are currently limited, may provide important insights into weathering profile development and clay formation processes. We also show that clay arrays in geologic datasets showing significant evaporative effects may be more useful in reconstructing ‘source’ water compositions than being used as a single mineral thermometer *a priori*. Further, since more clay formation happens in regions with mild to moderate evaporation and less chemical weathering likely happens in desert environments, accounting for potential biases in the preservation of different soil types and the differential systematics of this proxy system in wet, colder environments versus hot, dry systems will be important in future work. Additionally, future work pairing the modeling developed here to a reactive transport weathering framework for primary mineral dissolution, clay mineral formation and weathering front advance[77,80,84] will be necessary to fully describe the system.

To conclude, the work here demonstrates the effect of three processes previously not quantitatively considered but widely observed and acknowledged in modern systems: 1) surface temperature seasonality and covariation of temperature with meteoric water $\delta^{18}O$-$\delta^{2}H$ variations, 2) soil pore water evaporation, and 3) soil temperature variations with depth. We demonstrate, using both a forward model of modern soil pore waters and an inverse model of geologic data, how all three processes may play a role in the interpretation and utility of clay $\delta^{18}O$ and $\delta^{2}H$ datasets. While these effects have been discussed qualitatively or schematically and graphically in previous work[19,101], our work provides the first modeling framework to refine this methodology based on modern and paleo observations across a diversity of climatological locations and pedogenic settings where clays are formed.

References

1. Urey, H. C. The thermodynamic properties of isotopic substances. *J. Chem. Soc.* 562–581 (1947) doi:10.1039/JR9470000562.
2. DANSGAARD, W. Stable Isotopes in Precipitation. *Tellus* **16**, 436–468 (1964).
3. Gat, J. R. Oxygen and hydrogen isotopes in the hydrologic cycle. *Annu. Rev. Earth Planet. Sci.* **24**, 225–262 (1996).
4. Aggarwal, P. K., Gat, J. R. & Froehlich, K. F. O. Isotopes in the water cycle: Past, present and future of a developing science. *Isot. Water Cycle Past, Present Futur. a Dev. Sci.* 1–381 (2005) doi:10.1007/1-4020-3023-1/COVER.
5. Bowen, G. J., Cai, Z., Fiorella, R. P. & Putman, A. L. Isotopes in the Water Cycle: Regional- to Global-Scale Patterns and Applications. *Annu. Rev. Earth Planet. Sci.* **47**, 453–479 (2019).
6. Craig, H. Isotopic variations in meteoric waters. *Science (80-.).* **133**, 1702–1703 (1961).
7. Craig, H. & Gordon, L. I. Deuterium and oxygen-18 variations in the ocean and the marine atmosphere. in *Proceedings of a Conference on Stable Isotopes in Oceanographic Studies and Paleotemperatures* (ed. E Tongiorgi) 9–130 (1965).
8. GONFIANTINI, R. Environmental isotopes in lake studies. *Handb. Environ. Isot. Geochemistry* (1986).
9. Gonfiantini, R., Wassenaar, L. I., Araguas-Araguas, L. & Aggarwal, P. K. A unified Craig-Gordon isotope model of stable hydrogen and oxygen isotope fractionation during fresh or saltwater evaporation. *Geochim. Cosmochim. Acta* **235**, 224–236 (2018).
10. Aron, P. G. *et al.* Triple oxygen isotopes in the water cycle. *Chem. Geol.* **565**, 120026 (2021).
11. O’Neil, J. R., Clayton, R. N. & Mayeda, T. K. Oxygen Isotope Fractionation in Divalent Metal Carbonates. *J. Chem. Phys.* **51**, 5547–5558 (2003).
12. Capuano, R. M. The temperature dependence of hydrogen isotope fractionation between clay minerals and water: Evidence from a geopressured system. *Geochim. Cosmochim. Acta* **56**, 2547–2554 (1992).

13. Kim, S. T. & O’Neil, J. R. Equilibrium and nonequilibrium oxygen isotope effects in synthetic carbonates. *Geochim. Cosmochim. Acta* **61**, 3461–3475 (1997).
14. Savin, S. M. & Epstein, S. The oxygen and hydrogen isotope geochemistry of clay minerals. *Geochim. Cosmochim. Acta* **34**, 25–42 (1970).
15. O’Neil, J. R. & Kharaka, Y. K. Hydrogen and oxygen isotope exchange reactions between clay minerals and water. *Geochim. Cosmochim. Acta* **40**, 241–246 (1976).
16. Gilg, H. A. D–H evidence for the timing of kaolinization in Northeast Bavaria, Germany. *Chem. Geol.* **170**, 5–18 (2000).
17. Mora, G. & Pratt, L. M. Isotopic evidence for cooler and drier conditions in the tropical Andes during the last glacial stage. *Geology* **29**, 519–522 (2001).
18. Rosenau, N. A. & Tabor, N. J. Oxygen and hydrogen isotope compositions of paleosol phyllosilicates: Differential burial histories and determination of Middle–Late Pennsylvanian low-latitude terrestrial paleotemperatures. *Palaeogeogr. Palaeoclimatol. Palaeoecol.* **392**, 382–397 (2013).
19. Mix, H. T. & Chamberlain, C. P. Stable isotope records of hydrologic change and paleotemperature from smectite in Cenozoic western North America. *Geochim. Cosmochim. Acta* **141**, 532–546 (2014).
20. Hall, A. M., Gilg, H. A., Fallick, A. E. & Merritt, J. W. Kaolins in gravels and saprolites in north-east Scotland: Evidence from stable H and O isotopes for Palaeocene–Miocene deep weathering. *Palaeogeogr. Palaeoclimatol. Palaeoecol.* **424**, 6–16 (2015).
21. Mix, H. T., Ibarra, D. E., Mulch, A., Graham, S. A. & Chamberlain, C. P. A hot and high Eocene Sierra Nevada. *GSA Bull.* **128**, 531–542 (2016).
22. Gao, Z., Weng, H. & Guo, H. Unraveling influences of nitrogen cycling on arsenic enrichment in groundwater from the Hetao Basin using geochemical and multi-isotopic approaches. *J. Hydrol.* **595**, 125981 (2021).
23. Stern, L. A., Chamberlain, C. P., Reynolds, R. C. & Johnson, G. D. Oxygen isotope evidence of climate change from pedogenic clay minerals in the Himalayan molasse. *Geochim. Cosmochim. Acta* **61**, 731–744 (1997).
24. Tabor, N. J., Montanez, I. P. & Southard, R. J. Paleoenvironmental reconstruction from chemical and isotopic compositions of Permo-Pennsylvanian pedogenic minerals. *Geochim. Cosmochim. Acta* **66**, 3093–3107 (2002).
25. John, S. G., Mendez, J., Moffett, J. & Adkins, J. The flux of iron and iron isotopes from San Pedro Basin sediments. *Geochim. Cosmochim. Acta* **93**, 14–29 (2012).
26. Kukla, T. *et al.* High-Resolution Stable Isotope Paleotopography of the John Day Region, Oregon, United States . *Frontiers in Earth Science* vol. 9 at https://www.frontiersin.org/articles/10.3389/feart.2021.635181 (2021).
27. Vitali, F., Longstaffe, F. J., McCarthy, P. J., Plint, A. G. & Caldwell, W. G. E. Stable isotopic investigation of clay minerals and pedogenesis in an interfluve paleosol from the Cenomanian Dunvegan Formation, N.E. British Columbia, Canada. *Chem. Geol.* **192**, 269–287 (2002).
28. Gilg, H. A. *et al.* Genesis of amethyst geodes in basaltic rocks of the Serra Geral Formation (Ametista do Sul, Rio Grande do Sul, Brazil): a fluid inclusion, REE, oxygen, carbon, and Sr isotope study on basalt, quartz, and calcite. *Miner. Depos.* **38**, 1009–1025 (2003).
29. Sjostrom, D. J., Hren, M. T., Horton, T. W., Waldbauer, J. R. & Chamberlain, C. P. Stable isotopic evidence for a pre–late Miocene elevation gradient in the Great Plains–Rocky Mountain region, USA. in *Tectonics, Climate, and Landscape Evolution* (eds. Willett, S. D., Hovius, N., Brandon, M. T. & Fisher, D. M.) vol. 398 0 (Geological Society of America, 2006).
30. Gilg, H. A., Hall, A. M., Ebert, K. & Fallick, A. E. Cool kaolins in Finland. *Palaeogeogr. Palaeoclimatol. Palaeoecol.* **392**, 454–462 (2013).

31. Tabor, N. J. & Montañez, I. P. Oxygen and hydrogen isotope compositions of Permian pedogenic phyllosilicates: Development of modern surface domain arrays and implications for paleotemperature reconstructions. *Palaeogeogr. Palaeoclimatol. Palaeoecol.* **223**, 127–146 (2005).
32. Feng, W. & Yapp, C. J. 18O/16O and D/H ratios of pedogenic kaolinite in a North American Cenomanian laterite: Paleoclimatic implications. *Geochim. Cosmochim. Acta* **73**, 6249–6263 (2009).
33. Muttik, N., Kirsimäe, K. & Vennemann, T. W. Stable isotope composition of smectite in suevites at the Ries crater, Germany: Implications for hydrous alteration of impactites. *Earth Planet. Sci. Lett.* **299**, 190–195 (2010).
34. Meyer, I., Davies, G. R. & Stuut, J.-B. W. Grain size control on Sr-Nd isotope provenance studies and impact on paleoclimate reconstructions: An example from deep-sea sediments offshore NW Africa. *Geochemistry, Geophys. Geosystems* **12**, (2011).
35. Knauth, L. P. & Epstein, S. Hydrogen and oxygen isotope ratios in nodular and bedded cherts. *Geochim. Cosmochim. Acta* **40**, 1095–1108 (1976).
36. Kolodny, Y. & Epstein, S. Stable isotope geochemistry of deep sea cherts. *Geochim. Cosmochim. Acta* **40**, 1195–1209 (1976).
37. Abruzzese, M. J., Waldbauer, J. R. & Chamberlain, C. P. Oxygen and hydrogen isotope ratios in freshwater chert as indicators of ancient climate and hydrologic regime. *Geochim. Cosmochim. Acta* **69**, 1377–1390 (2005).
38. Ibarra, D. E., Kukla, T., Methner, K. A., Mulch, A. & Chamberlain, C. P. Reconstructing Past Elevations From Triple Oxygen Isotopes of Lacustrine Chert: Application to the Eocene Nevadaplano, Elko Basin, Nevada, United States . *Frontiers in Earth Science* vol. 9 at https://www.frontiersin.org/articles/10.3389/feart.2021.628868 (2021).
39. Yapp, C. J. Oxygen and hydrogen isotope variations among goethites (α-FeOOH) and the determination of paleotemperatures. *Geochim. Cosmochim. Acta* **51**, 355–364 (1987).
40. Yapp, C. J. Oxygen isotope effects associated with the solid-state α-FeOOH to α-Fe2O3 phase transformation. *Geochim. Cosmochim. Acta* **54**, 229–236 (1990).
41. Tabor, N. J., Yapp, C. J. & Montanez, I. P. Goethite, calcite, and organic matter from Permian and Triassic soils: carbon isotopes and CO2 concentrations. *Geochim. Cosmochim. Acta* **68**, 1503–1517 (2004).
42. Amin, A. *et al.* Depth distribution of soil water sourced by plants at the global scale: A new direct inference approach. *Ecohydrology* **13**, e2177 (2020).
43. Sprenger, M. *et al.* Storage, mixing, and fluxes of water in the critical zone across northern environments inferred by stable isotopes of soil water. *Hydrol. Process.* **32**, 1720–1737 (2018).
44. Benettin, P. *et al.* Effects of climatic seasonality on the isotopic \hack{\break} composition of evaporating soil waters. *Hydrol. Earth Syst. Sci.* **22**, 2881–2890 (2018).
45. Bowen, G. J. *et al.* Inferring the source of evaporated waters using stable H and O isotopes. *Oecologia* **187**, 1025–1039 (2018).
46. Knighton, J., Singh, K. & Evaristo, J. Understanding Catchment-Scale Forest Root Water Uptake Strategies Across the Continental United States Through Inverse Ecohydrological Modeling. *Geophys. Res. Lett.* **47**, (2020).
47. Oshun, J., Dietrich, W. E., Dawson, T. E. & Fung, I. Dynamic, structured heterogeneity of water isotopes inside hillslopes. *Water Resour. Res.* **52**, 164–189 (2016).
48. Simonin, K. A. *et al.* Vegetation induced changes in the stable isotope composition of near surface humidity. *Ecohydrology* **7**, 936–949 (2014).
49. Rempe, D. M. & Dietrich, W. E. A bottom-up control on fresh-bedrock topography under landscapes. *Proc. Natl. Acad. Sci. U. S. A.* **111**, 6576–6581 (2014).
50. Renée Brooks, J., Barnard, H. R., Coulombe, R. & McDonnell, J. J. Ecohydrologic

separation of water between trees and streams in a Mediterranean climate. *Nat. Geosci.* **3**, 100–104 (2010).

51. Evaristo, J., McDonnell, J. J., Scholl, M. A., Bruijnzeel, L. A. & Chun, K. P. Insights into plant water uptake from xylem-water isotope measurements in two tropical catchments with contrasting moisture conditions. *Hydrol. Process.* **30**, 3210–3227 (2016).
52. Hillel, D. *Introduction to soil physics*. (1982).
53. Zimmermann, U., MüNnich, K. O. & Roether, W. Downward Movement of Soil Moisture Traced by Means of Hydrogen Isotopes. in *Isotope Techniques in the Hydrologic Cycle* 28–36 (1967). doi:https://doi.org/10.1029/GM011p0028.
54. Delgado, A. & Reyes, E. Oxygen and hydrogen isotope compositions in clay minerals: A potential single-mineral geothermometer. *Geochim. Cosmochim. Acta* **60**, 4285–4289 (1996).
55. Sheppard, S. M. F. & Gilg, H. A. Stable isotope geochemistry of clay minerals: “The story of sloppy, sticky, lumpy and tough” Cairns-Smith (1971). *Clay Miner.* **31**, 1–24 (1996).
56. Savin, S. M. & Hsieh, J. C. C. The hydrogen and oxygen isotope geochemistry of pedogenic clay minerals: principles and theoretical background. *Geoderma* **82**, 227–253 (1998).
57. Savin, S. M. & Lee, M. Isotopic studies of phyllosilicates. *Rev. Mineral. Geochemistry* **19**, 189–223 (1988).
58. Brand, W. A. & Coplen, T. B. Stable isotope deltas: tiny, yet robust signatures in nature. *Isotopes Environ. Health Stud.* **48**, 393–409 (2012).
59. Bird, M. I., Longstaffe, F. J., Fyfe, W. S. & Bildgen, P. Oxygen-isotope systematics in a multiphase weathering system in Haiti. *Geochim. Cosmochim. Acta* **56**, 2831–2838 (1992).
60. Bird, M. I. & Chivas, A. R. Geomorphic and palaeoclimatic implications of an oxygen-isotope chronology for Australian deeply weathered profiles. *Aust. J. Earth Sci.* **40**, 345–358 (1993).
61. Dee, S. *et al.* Water isotopes, climate variability, and the hydrological cycle: recent advances and new frontiers. *Environ. Res. Clim.* **2**, 022002 (2023).
62. Rozanski, K., Araguás-Araguás, L. & Gonfiantini, R. Isotopic Patterns in Modern Global Precipitation. in *Climate Change in Continental Isotopic Records* 1–36 (1993). doi:https://doi.org/10.1029/GM078p0001.
63. Heitmann, E. O., Hyland, E. G., Schoettle-Greene, P., Brigham, C. A. P. & Huntington, K. W. Rise of the Colorado Plateau: A Synthesis of Paleoelevation Constraints From the Region and a Path Forward Using Temperature-Based Elevation Proxies . *Frontiers in Earth Science* vol. 9 at https://www.frontiersin.org/articles/10.3389/feart.2021.648605 (2021).
64. Kohn, M. J. & Welker, J. M. On the temperature correlation of δ18O in modern precipitation. *Earth Planet. Sci. Lett.* **231**, 87–96 (2005).
65. Dawson, T. E. & Simonin, K. A. The Roles of Stable Isotopes in Forest Hydrology and Biogeochemistry BT - Forest Hydrology and Biogeochemistry: Synthesis of Past Research and Future Directions. in (eds. Levia, D. F., Carlyle-Moses, D. & Tanaka, T.) 137–161 (Springer Netherlands, 2011). doi:10.1007/978-94-007-1363-5_7.
66. Gibson, J. J., Birks, S. J. & Edwards, T. W. D. Global prediction of δA and δ2H-δ18O evaporation slopes for lakes and soil water accounting for seasonality. *Global Biogeochem. Cycles* **22**, (2008).
67. Chamberlain, C. P., Winnick, M. J., Mix, H. T., Chamberlain, S. D. & Maher, K. The impact of neogene grassland expansion and aridification on the isotopic composition of continental precipitation. *Global Biogeochem. Cycles* **28**, 992–1004 (2014).
68. Barnes, C. J. & Allison, G. B. The distribution of deuterium and 18O in dry soils: 1. Theory. *J. Hydrol.* **60**, 141–156 (1983).

69. Fischer-Femal, B. J. & Bowen, G. J. Coupled carbon and oxygen isotope model for pedogenic carbonates. *Geochim. Cosmochim. Acta* **294**, 126–144 (2021).

70. Passey, B. H., Levin, N. E., Cerling, T. E., Brown, F. H. & Eiler, J. M. High-temperature environments of human evolution in East Africa based on bond ordering in paleosol carbonates. *Proc. Natl. Acad. Sci.* **107**, 11245–11249 (2010).

71. Quade, J., Eiler, J., Daëron, M. & Achyuthan, H. The clumped isotope geothermometer in soil and paleosol carbonate. *Geochim. Cosmochim. Acta* **105**, 92–107 (2013).

72. Gallagher, T. M., Hren, M. & Sheldon, N. D. The effect of soil temperature seasonality on climate reconstructions from paleosols. *Am. J. Sci.* **319**, 549–581 (2019).

73. Kelson, J. R. *et al.* A proxy for all seasons? A synthesis of clumped isotope data from Holocene soil carbonates. *Quat. Sci. Rev.* **234**, 106259 (2020).

74. Kukla, T. *et al.* Drier Winters Drove Cenozoic Open Habitat Expansion in North America. *AGU Adv.* **3**, e2021AV000566 (2022).

75. Chamberlain, C. P., Waldbauer, J. R. & Jacobson, A. D. Strontium, hydrothermal systems and steady-state chemical weathering in active mountain belts. *Earth Planet. Sci. Lett.* **238**, 351–366 (2005).

76. Ferrier, K. L. & Kirchner, J. W. Effects of physical erosion on chemical denudation rates: A numerical modeling study of soil-mantled hillslopes. *Earth Planet. Sci. Lett.* **272**, 591–599 (2008).

77. Brantley, S. L., White, A. F. & Kubicki, J. D. Kinetics of water-rock interaction. *Kinet. Water-Rock Interact.* 1–833 (2008) doi:10.1007/978-0-387-73563-4/COVER.

78. White, A. F. *et al.* Chemical weathering of a marine terrace chronosequence, Santa Cruz, California I: interpreting rates and controls based on soil concentration–depth profiles. *Geochim. Cosmochim. Acta* **72**, 36–68 (2008).

79. White, A. F. *et al.* Chemical weathering of a marine terrace chronosequence, Santa Cruz, California. Part II: Solute profiles, gradients and the comparisons of contemporary and long-term weathering rates. *Geochim. Cosmochim. Acta* **73**, 2769–2803 (2009).

80. Maher, K., Steefel, C. I., White, A. F. & Stonestrom, D. A. The role of reaction affinity and secondary minerals in regulating chemical weathering rates at the Santa Cruz Soil Chronosequence, California. *Geochim. Cosmochim. Acta* **73**, 2804–2831 (2009).

81. Hewawasam, T. *et al.* Slow advance of the weathering front during deep, supply-limited saprolite formation in the tropical Highlands of Sri Lanka. *Geochim. Cosmochim. Acta* **118**, 202–230 (2013).

82. Druhan, J. L. & Maher, K. A Model Linking Stable Isotope Fractionation to Water Flux and Transit Times in Heterogeneous Porous Media. *Procedia Earth Planet. Sci.* **10**, 179–188 (2014).

83. Behrens, R. *et al.* Mineralogical transformations set slow weathering rates in low-porosity metamorphic bedrock on mountain slopes in a tropical climate. *Chem. Geol.* **411**, 283–298 (2015).

84. Winnick, M. J., Druhan, J. L. & Maher, K. Weathering intensity and lithium isotopes: A reactive transport perspective. *Am. J. Sci.* **322**, 647–682 (2022).

85. Maher, K. The dependence of chemical weathering rates on fluid residence time. *Earth Planet. Sci. Lett.* **294**, 101–110 (2010).

86. Evaristo, J., McDonnell, J. J., Scholl, M. A., Bruijnzeel, L. A. & Chun, K. P. Insights into plant water uptake from xylem-water isotope measurements in two tropical catchments with contrasting moisture conditions. *Hydrol. Process.* n/a-n/a (2016) doi:10.1002/hyp.10841.

87. Al-Ani, T., Sarapää, O. & Lehtinen, M. J. Mineralogical and chemical study of some kaolin samples from the Kahdeksaisiensuo and Hyväjärvi occurrences, Virtasalmi, SE Finland. Geological Survey of Finland. in *Geological Survey of Finland, Report M19/3232/2006/1/822010, Espoo* 19 (2006).

88. Lintinen, P. *Kaoliinitutkimukset Sodankylän Kelujärven ympäristössä 2003–2004*. (2006) doi:Report M19/3713,3714,3731,3732/2006/1/82.
89. Ingraham, N. L. & Taylor, B. E. Light stable isotope systematics of large-scale hydrologic regimes in California and Nevada. *Water Resour. Res.* **27**, 77–90 (1991).
90. Speelman, E. N. *et al.* Modeling the influence of a reduced equator-to-pole sea surface temperature gradient on the distribution of water isotopes in the Early/Middle Eocene. *Earth Planet. Sci. Lett.* **298**, 57–65 (2010).
91. Mulch, A., Graham, S. A. & Chamberlain, C. P. Hydrogen Isotopes in Eocene River Gravels and Paleoelevation of the Sierra Nevada. *Science (80-.).* **313**, 87–89 (2006).
92. Cassel, E. J. & Graham, S. A. Paleovalley morphology and fluvial system evolution of Eocene–Oligocene sediments (“auriferous gravels”), northern Sierra Nevada, California: Implications for climate, tectonics, and topography. *GSA Bull.* **123**, 1699–1719 (2011).
93. Henry, C. D. *et al.* Eocene–Early Miocene paleotopography of the Sierra Nevada–Great Basin–Nevadaplano based on widespread ash-flow tuffs and paleovalleys. *Geosphere* **8**, 1–27 (2012).
94. Cassel, E. J., Breecker, D. O., Henry, C. D., Larson, T. E. & Stockli, D. F. Profile of a paleo-orogen: High topography across the present-day Basin and Range from 40 to 23 Ma. *Geology* **42**, 1007–1010 (2014).
95. Cassel, E. J., Graham, S. A. & Chamberlain, C. P. Cenozoic tectonic and topographic evolution of the northern Sierra Nevada, California, through stable isotope paleoaltimetry in volcanic glass. *Geology* **37**, 547–550 (2009).
96. Hren, M. T., Pagani, M., Erwin, D. M. & Brandon, M. Biomarker reconstruction of the early Eocene paleotopography and paleoclimate of the northern Sierra Nevada. *Geology* **38**, 7–10 (2010).
97. Mulch, A. Stable isotope paleoaltimetry and the evolution of landscapes and life. *Earth Planet. Sci. Lett.* **433**, 180–191 (2016).
98. Evans, M. N., Tolwinski-Ward, S. E., Thompson, D. M. & Anchukaitis, K. J. Applications of proxy system modeling in high resolution paleoclimatology. *Quat. Sci. Rev.* **76**, 16–28 (2013).
99. Dee, S. G., Russell, J. M., Morrill, C., Chen, Z. & Neary, A. PRYSM v2.0: A Proxy System Model for Lacustrine Archives. *Paleoceanogr. Paleoclimatology* **33**, 1250–1269 (2018).
100. Bowen, G. J., Fischer-Femal, B., Reichart, G.-J., Sluijs, A. & Lear, C. H. Joint inversion of proxy system models to reconstruct paleoenvironmental time series from heterogeneous data. *Clim. Past* **16**, 65–78 (2020).
101. Grujic, D. *et al.* Formation of a Rain Shadow: O and H Stable Isotope Records in Authigenic Clays From the Siwalik Group in Eastern Bhutan. *Geochemistry, Geophys. Geosystems* **19**, 3430–3447 (2018).

Acknowledgements

Ibarra acknowledges Page Chamberlain, Matthew Winnick, Jeremy Caves Rugenstein, Tyler Kukla and Kate Maher for discussions on this topic that informed this work. Evaristo acknowledges the support of Copernicus Institute for Sustainable Development, Utrecht University, for their support in making the research visit to Brown University possible.

Author contributions

Both authors conceived of this work jointly, created the figures and wrote the manuscript.

Competing interests

The authors declare no competing interests.

Data Availability

No new data was collected as part of this study.

Code Availability

All code and input files to reproduce the figures and analysis are provided as supplemental materials.

Figures and Figure Captions

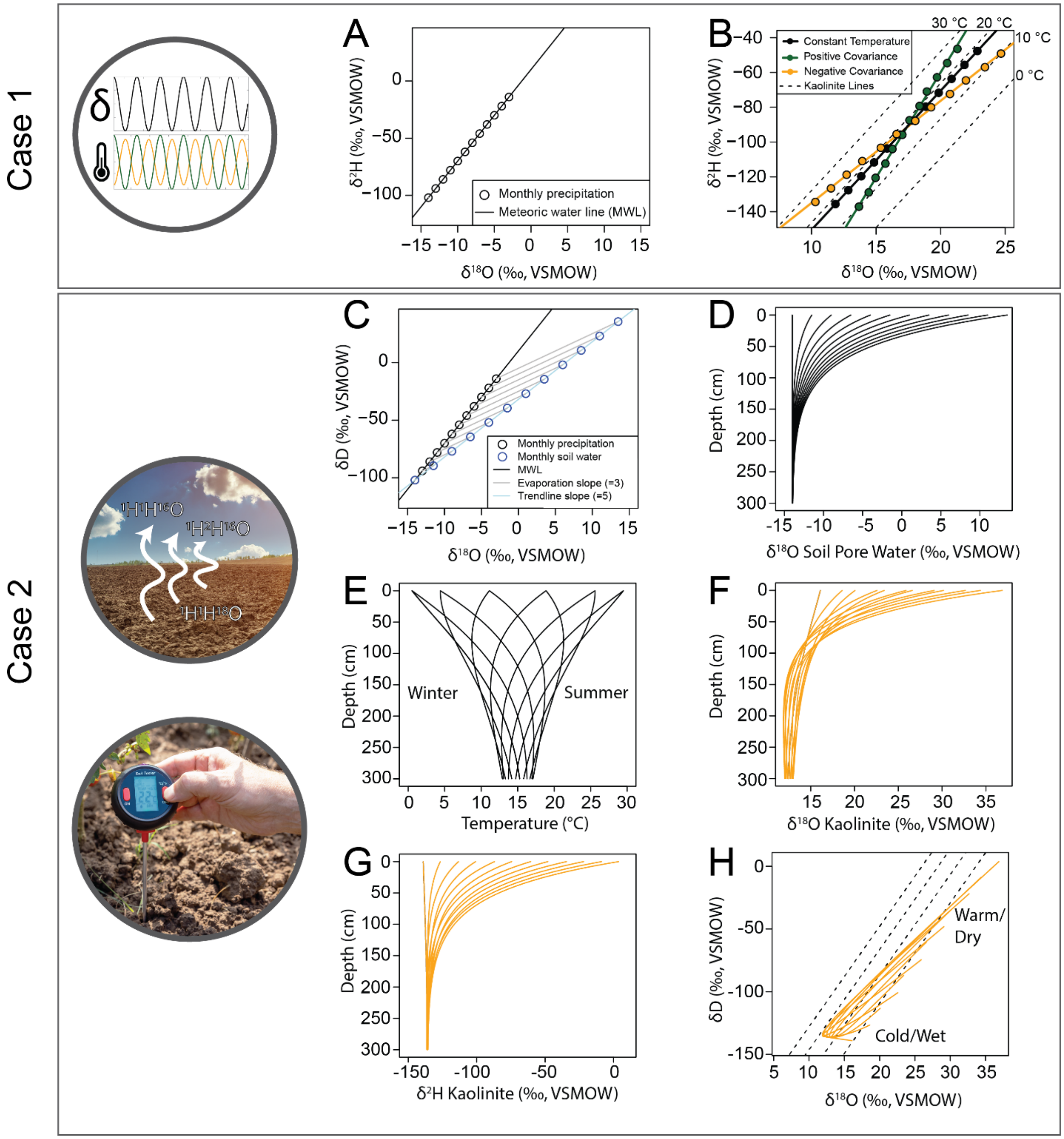

Figure 1. Conceptual framework for projection and interpretation of clay stable isotope data. A) Monthly precipitation values (black circles) falling along the global meteoric water line (MWL). **B)** Impact of seasonal temperature variations on waters falling along the MWL in A) for constant temperature, positive covariance and negative covariance between the isotopic composition of water and assumed fractionation temperatures (equations 7 and 8). A) and B) illustrate Case 1; inset in Case 1 shows the assumed variations in seasonal meteoric water isotopic compositions temperature depicted in B). **C)** As in A) and with monthly evaporation

slopes of 3 (gray line) intercepting an empirical slope (‘trendline’) of 5 (blue circles, light blue line). Evaporation slope of 3 was assumed for illustration purposes using the algorithm of Benettin et al. (2018). **D)** Monthly soil pore water oxygen isotopic composition as a function of depth (equation 5). **E)** Monthly propagation of seasonal temperature fluctuations with depth in a soil profile (equation 6). **F)** Calculated monthly kaolinite $\delta^{18}O$ in equilibrium with soil pore water and monthly temperature depth trends (equation 5). **G)** As in E) for kaolinite $\delta^{2}H$. **H)** Cross plot of monthly kaolinite $\delta^{18}O$-$\delta^{2}H$ (E and F) overlaid on status quo kaolinite lines (as in Box 1). C-H illustrate Case 2.

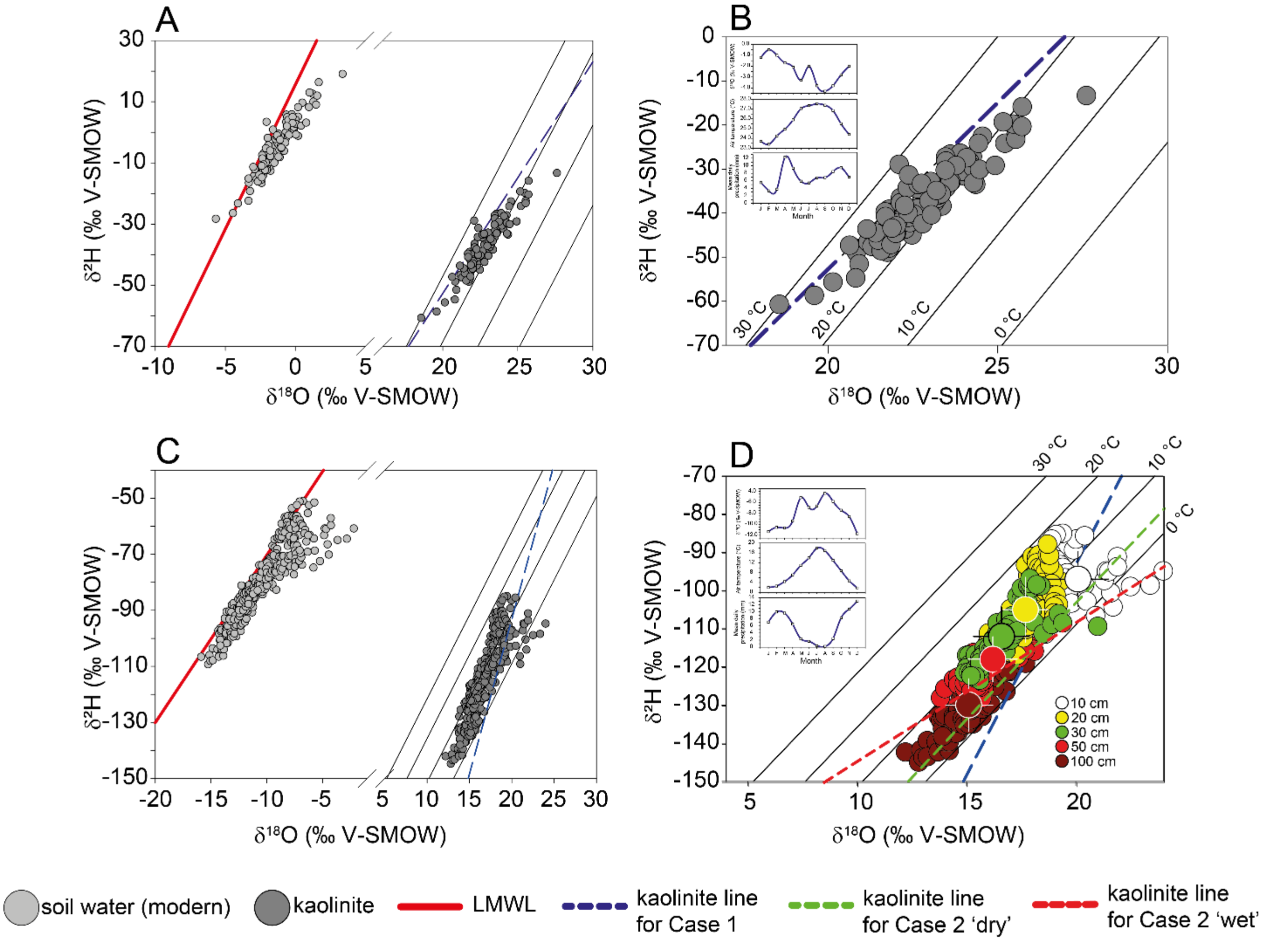

Figure 2. $\delta^{18}O$-$\delta^{2}H$ crossplots showing the application of the forward model to two modern soil water profiles. A) Modern soil water (filled light gray circles) and calculated kaolinite (filled dark gray circles) isotopic compositions in Luquillo, Puerto Rico (data from ref. 50; all else see Table S1). The solid red line represents the local meteoric water line (LMWL, $\delta^{2}H = 9.4\ \delta^{18}O + 15.5$). The dashed blue line represents a regression through calculated kaolinite isotopic compositions, informed by monthly variability in air temperature and precipitation $\delta^{18}O$ and $\delta^{2}H$ (as in Figure 1B, Case 1). The slope of the dashed blue line in B is 7.6. **B)** Magnified view of the clay lines region in A, showing the kaolinite formation temperatures 0°C, 10°C, 20°C, and 30°C; inset shows mean monthly values of precipitation $\delta^{18}O$ (top), air temperature (middle), and daily precipitation (bottom). **C)** As in A for Corvallis, Oregon (data from ref. 50; all else see Table S1) (LMWL, $\delta^{2}H = 5.9\ \delta^{18}O - 10.7$). **D)** As in B;

calculated kaolinite isotopic compositions are presented per soil depth; larger circles and error bars represent mean and 1σ, respectively; raw values are also shown in corresponding soil depth colors. The dashed green (slope 6.1) and red (slope 3.6) lines represent the trendlines through calculated kaolinite isotopic compositions, informed by monthly variability in soil depth-dependent temperature (as in Figure 1H, Case 2) for 'dry' and 'wet' seasons, respectively, constrained by evaporation line slope (3.4) and maximum isotopic compositions of residual soil water derived from the Craig-Gordon model (using the algorithm of ref. 44). The slope of the dashed blue line in D is 11.

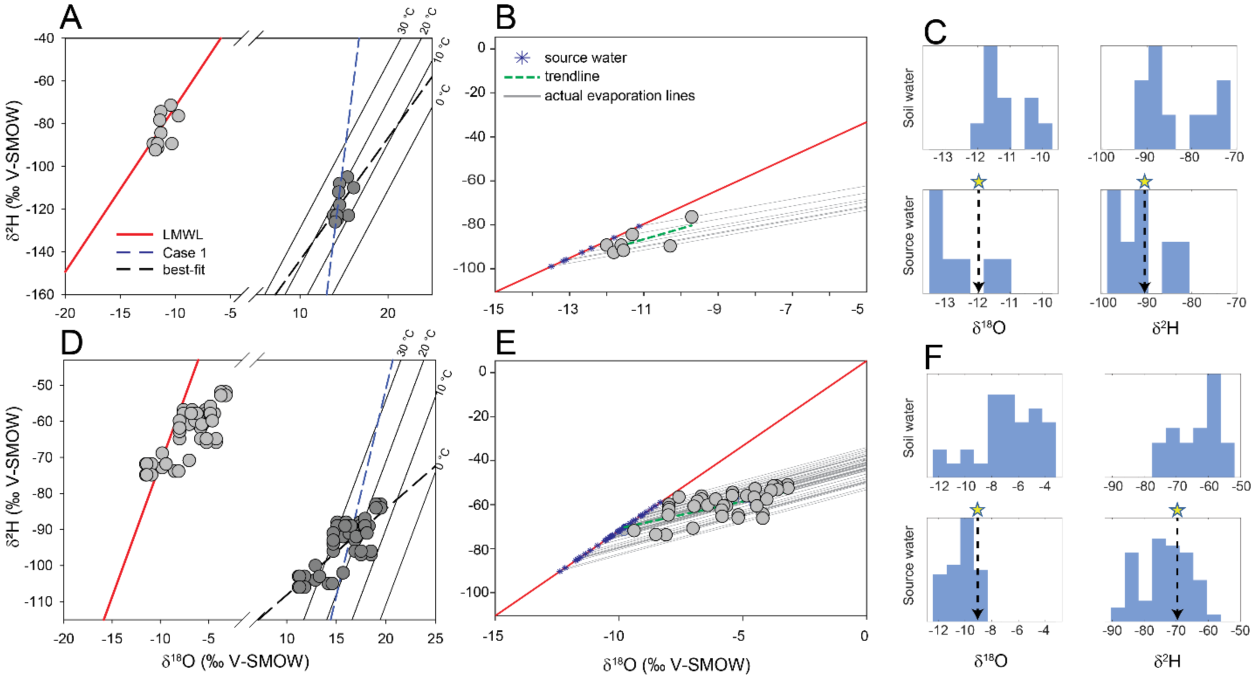

Figure 3. $\delta^{18}O$-$\delta^{2}H$ crossplots showing the application of the inverse model to two paleo soils. A) Calculated modern soil water (filled light gray circles) and measured kaolinite (filled dark gray circles) isotopic compositions in Finland (data from ref. 30; all else see Table S2). Calculated modern soil water assumes a soil temperature of 18°C, 16°C warmer than modern day long-term (1991-2021) air temperature at Rovaniemi, Finland. The solid red line represents the local meteoric water line (LMWL, $\delta^{2}H = 7.7\ \delta^{18}O + 5.4$). The dashed blue line (denoted as Case 1) represents a linear model, informed by monthly variability in precipitation $\delta^{18}O$ and $\delta^{2}H$ and modern day air temperature (slope 32). The dashed black line represents a linear best-fit to the measured kaolinite data (slope 5.7). Also shown are the kaolinite formation temperatures 0°C, 10°C, 20°C, and 30°C. **B)** Magnified region in A, showing how each calculated modern soil water is traced back to LMWL to determine the source water isotopic composition. Each soil water is assumed to have evaporated along a soil evaporation slope of 3. **C)** Histograms of calculated soil water and precipitation source water $\delta^{18}O$ and $\delta^{2}H$. The star symbols and dashed lines represent the isotopic compositions of precipitation source waters using the approach of simply running a trendline across all soil water data demonstrating an overestimate, particularly with respect to $\delta^{18}O$. **D)** As in A for sites in the Sierras (data from ref. 21; all else see Table S2). The solid red line represents the LMWL ($\delta^{2}H = 7.3\ \delta^{18}O + 1.5$). The slope of the dashed blue line (Case 1) is 11.5. The slope of the dashed black line (best-fit) is 2.4. Calculated modern soil

water assumes a soil temperature of 33°C, 22°C warmer than modern day long-term (1991-2021) air temperature at Auburn, California. **E)** As in B for sites in the Sierras. **F)** As in C for sites in the Sierras.

Supplementary Information for
"Soil pore water evaporation and temperature influences on clay mineral paleothermometry"

Daniel E.Ibarra[1,2] and Jaivime Evaristo[3]

1. Institute at Brown for Environment and Society, Brown University, Providence, RI, 02906 USA
2. Department of Earth, Environmental and Planetary Science, Brown University, Providence, RI, 02906 USA
3. Copernicus Institute of Sustainable Development, Utrecht University, Utrecht, The Netherlands

This Supplementary Information (S.I.) presented below elaborates further on the rationale and methodology that underpin the study as well as providing associated caveats and limitations where further model development may be necessary. We first provide a derivation of the status quo equations, demonstrate the effect of the fractionation factor approximation that is commonly used, describe caveats and limitations of the three cases presented in the main text, and elaborate on assumptions made in the forward and inverse modeling approaches used as examples in this work. R code to implement the thought experiments and calculations in Box 1, Figure S1, S2 and S3, and MATLAB to implement the forward and inverse model calculations are provided as supplementary files.

Extended Methods

I. Derivation of status quo paleothermometry equations

While previous work has presented abbreviated derivations of the clay mineral thermometers based on hydrogen and oxygen isotopes[14, 22, 26, 27, 29, 47] the mathematical operations required to go from two fractionation factor equations and the meteoric water line (equations 1 and 2) to the single mineral thermometry equations (equations 3 and 4) are not formally derived in the peer review literature. For completeness we do so here using kaolinite as the example mineral. Starting from the kaolinite fractionation factors from ref. 55 for oxygen:

$$1000 \times \ln\alpha_{\text{kaol-water-O}} = 2.76\text{x}10^{6} \times T^{-2} - 6.75 \qquad \text{(S1)}$$

and for hydrogen:

$$1000 \times \ln\alpha_{\text{kaol-water-H}} = -2.2\text{x}10^{6} \times T^{-2} - 7.7 \qquad \text{(S2).}$$

Then taking the global meteoric water line as our third constraint:

$$\delta^{2}H = 8\text{x}\delta^{18}O + 10 \qquad \text{(S3),}$$

and the approximation for 1000lnα (see next section) as the difference between two phases, we are left with the following two equations:

$$\delta^{18}O_{kaol} - \delta^{18}O_{sw} = 2.76x10^{6} \text{ x } T^{-2} - 6.75 \quad (S4)$$

and

$$\delta^{2}H_{kaol} - \delta^{2}H_{sw} = -2.2x10^{6} \text{ x } T^{-2} - 7.7 \quad (S5).$$

Assuming waters fall along the meteoric water line (a key assumption questioned by this work), and plugging equations 4 and 5 into the GMWL, equation 3, gives the following expanded equation:

$$\delta^{2}H_{kaol} + 2.2x10^{6} \text{ x } T^{-2} - 7.7 = 8*(\delta^{18}O_{kaol} - 2.76x10^{6} \text{ x } T^{-2} - 6.75) + 10 \quad (S6).$$

Rearranging for 10^{6} x T^{-2} and simplifying terms leads to equation 3 from the main text:

$$3.0350 \text{ x } 10^{6}T^{-2} = \delta^{18}O_{kaolinite} -0.1250x\delta^{2}H_{kaolinite} + 7.0375 \quad (S7).$$

The analogous derivation holds for smectite[54].

II. Approximation of 1000lnα = δ_{clay} - δ_{sw}

A commonly used assumption to simplify mathematical operations in isotope geochemistry is that 1000lnα is the difference between two phases. In the case of clay mineral thermometry this approximation is between the clay mineral and the source water (equations 7 and 8). This approximation breaks down at extremely large fractionation factors (i.e. >100‰) because the mole fraction of the minor isotope is non-linear with the delta notation (as defined and used by the field; e.g., ref. 58). As such, the exact expression for the fractionation factor (α), based on the isotopic ratios (R) are described as:

$$^{18}\alpha_{kaol\text{-}water} = {}^{18}R_{kaol} / {}^{18}R_{sw} = (\delta^{18}O_{kaol} + 1000) / (\delta^{18}O_{sw} + 1000) \quad (S8)$$

$$^{2}\alpha_{kaol\text{-}water} = {}^{2}R_{kaol} / {}^{2}R_{sw} = (\delta^{2}H_{kaol} + 1000) / (\delta^{2}H_{sw} + 1000) \quad (S9)$$

As discussed in the main text $^{18}\alpha_{kaol\text{-}water}$ is greater than 1 and $^{2}\alpha_{kaol\text{-}water}$ is less than 1 resulting in clay minerals falling below and to the right of the GMWL or LMWL in $\delta^{18}O$-$\delta^{2}H$ crossplot space. In Figure S1 we demonstrate the consequence of this inaccuracy caused by the commonly used approximation by plotting clay lines produced from the precise expression (equations S8 and S9) versus the approximation (equations 7 and 8). Across Earth's surface temperatures and typical meteoric water values (Fig. S1A), inaccuracies in the calculated temperature are typically <2 °C, and are dependent on both the temperature of formation and the initial source water's isotopic composition (Fig. S1B).

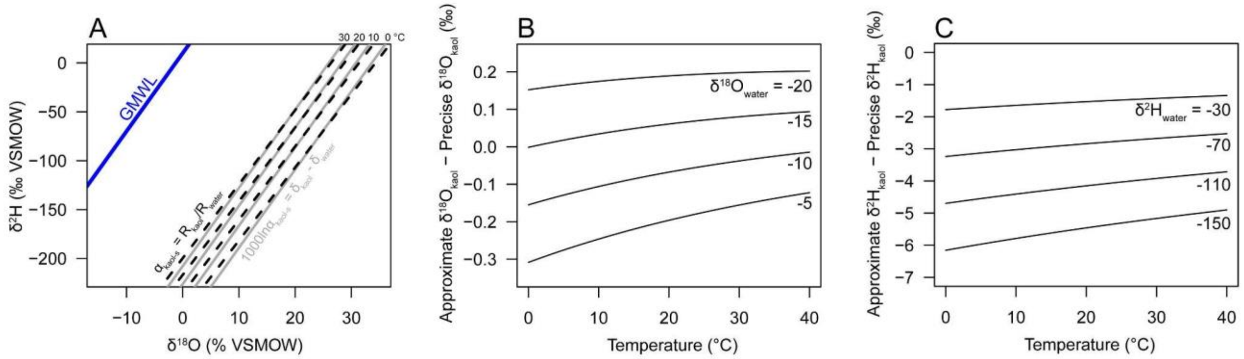

Figure S1. Sensitivity of calculations to 1000lnα = δ_{clay} - δ_{sw} approximation. **A)** Fractionation of global meteoric water line (blue line) to clay lines at 0 to 30 °C using the 1000lnα = δ_{clay} - δ_{sw} (as typically assumed; gray lines) compared to the precise definition for α (Equations 8 and 9). **B)** Difference between the approximate and precise fractionation formulations with respect to kaolinite $\delta^{18}O$ values for a given source water composition as a function of temperature. **C)** As in B) for $\delta^{2}H$.

III. Elaboration on assumptions and limitations

In the following sections we elaborate on a few assumptions and limitations associated with the effects described in the main text. We also provided additional contextual figures associated with the calculations.

Case 1. The role of seasonal co-variations of temperature and meteoric water isotopic composition

The amount and isotopic compositions of precipitation are known to display both positive and negative covariation with temperature depending on the region and season[62]. In tropical areas, a negative covariation tends to occur during monsoon rainfall due to the 'amount effect' (e.g., ref. 5). Mid- to high-latitudes, however, tend to exhibit positive covariation as factors such as moisture source, humidity, and temperature change[62]. Case 1 isolates the impact of these seasonal covariations on single-mineral clay thermometers without the inclusion of soil pore water evaporation or temperature variations (Figure S2).

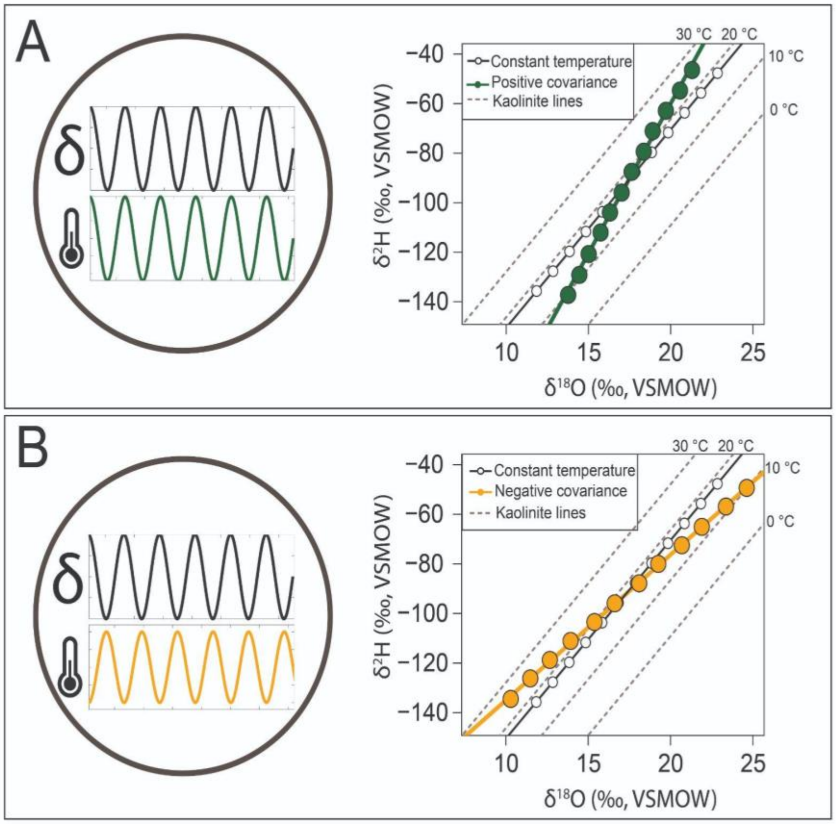

Figure S2. Impact of seasonal temperature variations of waters falling along the meteoric water line (MWL) on clay formation isotopic compositions as shown in Figure 1B. **A)** The case where precipitation isotopic compositions and monthly air temperatures are positively correlated. **B)** The case where precipitation isotopic compositions and monthly air temperatures are negatively correlated. Images in enclosed circles are illustrative depictions of the two cases. White circles in both panels represent the constant temperature case.

In Figure S3 we calculate the end-member evaporatively enriched waters (blue circles in Figure 1A) with positive and negative seasonality with respect to temperature variations. This does not yet resolve depth-dependent behavior but rather the maximum impact of surface temperature variations leading to changes in the clay line slope formed from evaporatively enriched waters. As in Figure S2 these assumed slopes are purely for illustrative purposes. With no seasonality of temperature imposed the result is that as water samples and the calculated clay line move away from the meteoric water line (i.e. have a lower d-excess value) the calculated clay values fall across the status quo contour lines (blue points, Figure 1A). Imposing a positive (negative) relationship between isotopic composition of precipitation and temperature results in steeping (shallowing) of slopes (green and orange points) rotated around the no temperature seasonality case. The trajectories shown in Figure 1C represent potential maximum cases, which if taken at face value with the status quo thermometry calculations would give temperatures dominantly less than freezing in the scenario described here. Incorporating the depth dependent trends in soil pore water stable isotopes and temperature fluctuations.

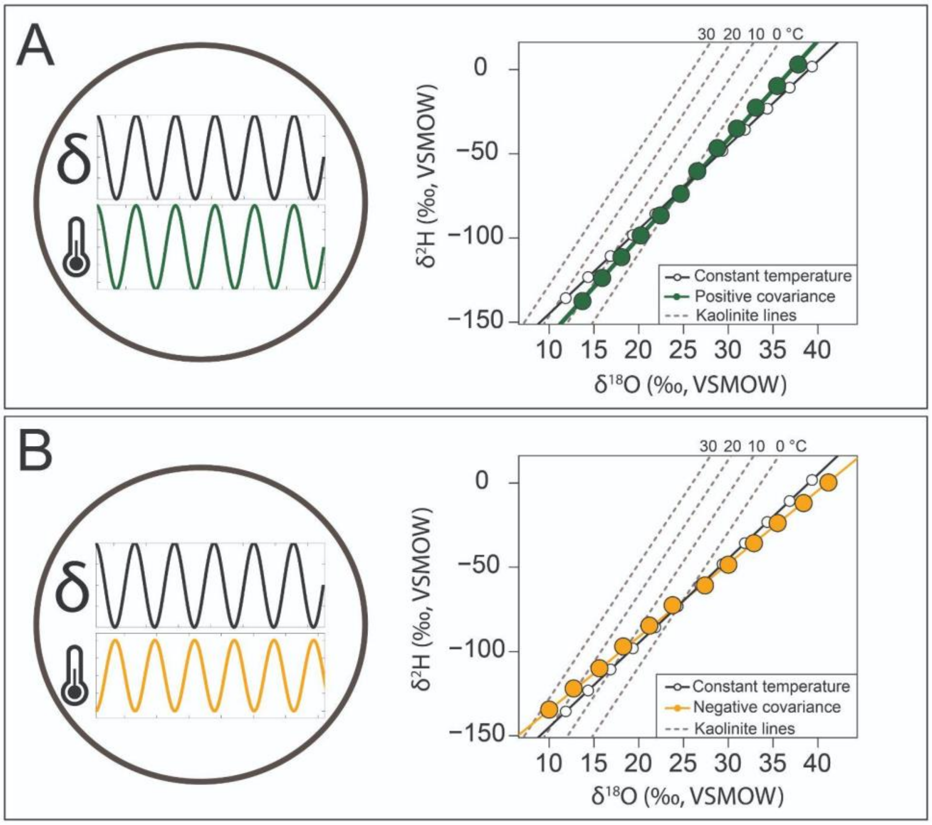

Figure S3. Impact of seasonal temperature variations of evaporated waters (see blue circles in Figure 1A of main text) on clay formation isotopic compositions. **A)** The case where precipitation isotopic compositions and monthly air temperatures are positively correlated. **B)** The case where precipitation isotopic compositions and monthly air temperatures are negatively correlated. Images in enclosed circles are illustrative depictions of the two cases. White circles in both panels represent the constant temperature case.

Case 2: The role of evaporatively enriched soil waters

For the purposes of determining the isotopic composition of soil minerals, as modeled in this work, this formulation does not account for the presence of the vapor phase in the upper most unsaturated zone in a soil that causes a decrease in $\delta^{18}O$ and $\delta^{2}H$ in the upper few centimeters[53, 67, 68]. It is most likely that a majority of clay mineral formation occurs below these depths [where evaporation predominates] based on weathering front profiles from chronosequences (e.g., ref. 80), justifying this simplifying assumption.

IV. Applications. Forward and inverse models

Forward model. We use measured modern soil pore water $\delta^{18}O$ and $\delta^{2}H$ ($\delta^{18}O_{sw}$ and $\delta^{2}H_{sw}$, respectively) as input to calculate $\delta^{18}O$ and $\delta^{2}H$ values of kaolinite ($\delta^{18}O_{kaol}$ and $\delta^{2}H_{kaol}$, respectively) as output. $\delta^{18}O_{sw}$ and $\delta^{2}H_{sw}$ are obtained from two published studies in Luquillo, Puerto Rico[86] and Corvallis, Oregon[50]. The results are visualized in Figure 2 of the main text.

See MATLAB codes and pertinent input files used to calculate $\delta^{18}O_{kaol}$ and $\delta^{2}H_{kaol}$. Note that the MATLAB code (Forward.mlx) generates Figure 2, including the LMWL and a trendline through all calculated kaolinite isotopic compositions (Case 1). Case 2 simulation (soil evaporation/Zimmerman equations) is written in R code.

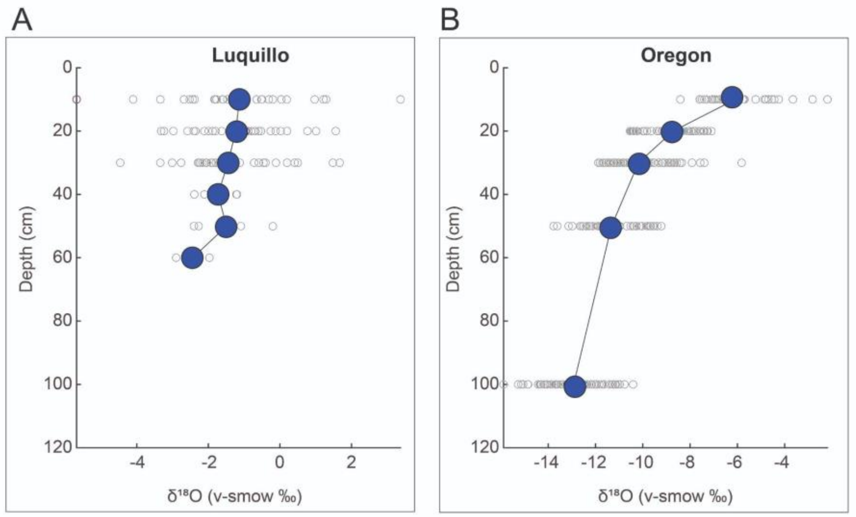

Figure S4. Soil pore water $\delta^{18}O$ depth profile for **A)** Luquillo and **B)** Oregon. Open gray circles represent pore water $\delta^{18}O$ data with depth. Filled circles represent corresponding mean values, connected by a line for emphasis. Note that the scales on the x-axis are not the same for both plots.

We underline a caveat in interpreting the Luquillo and Oregon soil pore water datasets. Figure S4 shows an apparent depth trend in the Oregon dataset. That is, soil pore water $\delta^{18}O$ decreases exponentially with depth. An empirical fit to the data (fit not shown) is approximated by a two-parameter exponential regression (R^2 0.994, RMSE 3.11). A decrease in soil pore water $\delta^{18}O$ with depth is a relatively common observation in settings with pronounced seasonality (e.g., ref. 102) and in soils undergoing evaporation[68]. The site in Oregon is in a Mediterranean climate with relatively strong precipitation and temperature seasonality. In kaolinite (clay formation) space (see Figure 2D in main text), the apparent depth trend at Oregon manifests as warmer clay formation temperatures closer to the surface, except at 10 cm. No such apparent depth trend exists in the Luquillo dataset, perhaps because Luquillo is considerably less seasonal than Oregon, or other sites where isotopic depletion of soil pore water with depth has been documented.

Another caveat that we underline in interpreting the Luquillo and Oregon soil pore water datasets is that our work assumes fidelity of soil pore water extraction techniques. Pore waters from both Luquillo and Oregon soil samples were reported to have been extracted using cryogenic vacuum distillation (CVD) technique[103]. In laboratory spiking experiments that subjected soils to extended high-temperature oven drying, some researchers have raised potential issues associated with the CVD technique’s ability to extract the ‘true’ soil pore water isotopic compositions[104-106]. Other researchers, however, have questioned the transferability of findings from laboratory experiments to soils under natural conditions. For example, ref. 107 and 108 showed that in field studies whereby soils have not been subjected to the same conditions, the CVD technique could reliably reproduce the isotopic compositions of the original source water. In light of the ongoing debate in the literature regarding the fidelity of the CVD technique, our work assumes that CVD is a reliable extraction technique for field soils, consistent with the determination made by ref 117.

Finally, we calculate depth-associated soil temperatures using Hillel's heat diffusion equation that includes a sinusoidal term, accounting for seasonal temperature fluctuations (ref. 52; Equation 6 in main text). For Luquillo, we use wet and dry season air temperatures of 26.8 and 25.1 °C, respectively [the two sampling points in ref. 86], as inputs to model the soil temperatures at corresponding $\delta^{18}O_{sw}$ and $\delta^{2}H_{sw}$ sampling depths. For Oregon, we use the mean annual temperature of 8.7 °C. Given that modeling $\delta^{18}O_{kaol}$ and $\delta^{2}H_{kaol}$ is sensitive to temperature (Equations S4 and S5), we emphasize that our assumptions that go into calculating depth-associated soil temperatures[52] are general approximations that may not be realistic (Figure S5). In the absence of measured soil temperatures with depth, our approach here must be treated purely as a first-order approximation. Future work could focus on *in situ* measurements of soil temperature at various depths in the soil profile.

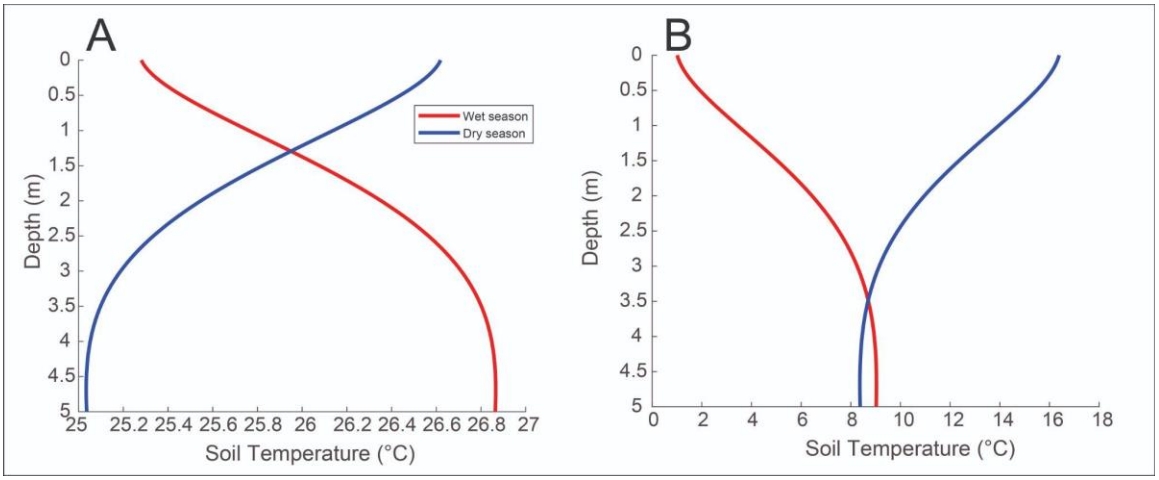

Figure S5. Modeled soil temperature profiles at respective sites in **A)** Luquillo and **B)** Oregon.

Inverse model. We use $\delta^{18}O_{kaol}$ and $\delta^{2}H_{kaol}$ data to predict the plausible values of $\delta^{18}O_{sw}$ and $\delta^{2}H_{sw}$ that best explain the observed kaolinite observations. $\delta^{18}O_{kaol}$ and $\delta^{2}H_{kaol}$ are obtained from two published studies in Finland[30] and the Sierras in western United States[21]. The results are visualized in Figure 3 of the main text. See MATLAB codes and pertinent input files used to calculate $\delta^{18}O_{sw}$ and $\delta^{2}H_{sw}$.

To model $\delta^{18}O_{sw}$ and $\delta^{2}H_{sw}$ using measured $\delta^{18}O_{kaol}$ and $\delta^{2}H_{kaol}$ (Equations S4 and S5), several soil temperature values were assumed. The solutions to the inverse problem are constrained by the relatively well-constrained physics of covariations on or below the LMWL (alternatively, GMWL). That is, $\delta^{18}O_{sw}$ and $\delta^{2}H_{sw}$ plotting 'on' the LMWL, by definition, approximate meteoric water isotopic compositions. Whereas, $\delta^{18}O_{sw}$ and $\delta^{2}H_{sw}$ plotting 'below' the LMWL indicate evaporative isotopic enrichment. We therefore consider as unrealistic any calculated $\delta^{18}O_{sw}$ and $\delta^{2}H_{sw}$ that fall ‘above’ the LMWL, which would otherwise represent the isotopic composition of the evaporate.

In Figure S6A, we see that if we assume a soil temperature of ~11 °C (which is similar to the long-term average air temperature of Auburn, CA), the modern soil pore waters are shown to be above the LMWL on the ‘evaporate space’. On the other hand, assuming a soil temperature of 50 °C shows that the soil pore waters are too enriched due to evaporation. Such a temperature would be unreasonably warm even for Eocene hothouse conditions (cf. ref. 21). However, if we assume a soil temperature of 33 °C, the soil pore waters plot close to the LMWL. We consider this to be more realistic than the other two extreme temperatures. Nevertheless, some data points still plot on the evaporate space (Figure S6B). We assume that these points are unrealistic values from which kaolinite would have formed. Thus, considering only the data points that plot on or below the LMWL, we determine the source waters of each modeled soil pore water (Figure S6C). That is, the meteoric water from which the clay mineral would have formed.

In tracing the source water isotopic composition, we assume that each calculated soil pore water must have evaporated along a soil evaporation line (SEL), following the approach of ref. 44. Figure S6C assumes an SEL slope of 3, close to the slopes of between 2 and 3 reported by ref. 55, and 3.1-3.4 reported by ref. 44. The approach of ref. 44 is a departure from the ‘trendline approach’ of earlier studies[109-113], which assumed that all evaporated waters originate from a single source water. The trendline approach is represented by the dashed black line in Figure S6C. In the absence of *a priori* and/or plausible information to inform an assumption that all evaporated soil pore waters originate from a single source water, we follow the mechanistic and more plausible approach of ref. 44.

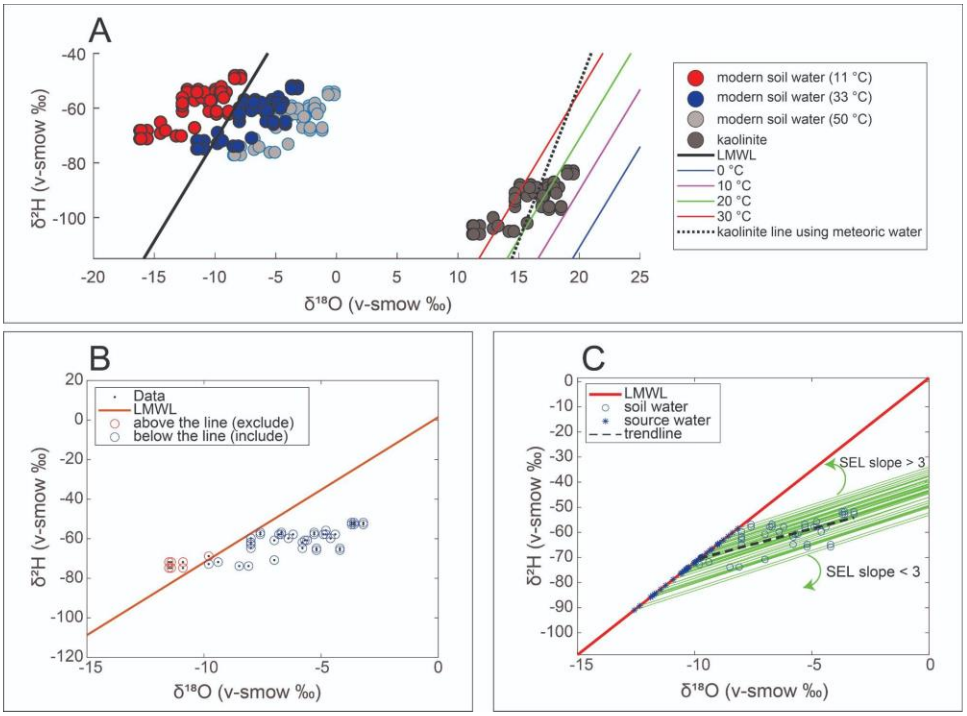

Figure S6. Determining source water isotopic compositions. **A)** Sensitivity of modeled $\delta^{18}O_{sw}$ and $\delta^{2}H_{sw}$ to various temperature assumptions (11, 33, 50 °C). **B)** Any calculated $\delta^{18}O_{sw}$-$\delta^{2}H_{sw}$ pair that plots above the LMWL are excluded from the determination of source water isotopic compositions. **C)** Tracing source water isotopic compositions as the intersection between the soil evaporation line and the LMWL, constrained by the soil evaporation line (SEL) slope (here set at 3). The effects of SEL slopes greater than or less than 3 are represented by the direction of the green arrows. The 'trendline approach' is represented by the dashed black line (slope = 2.5 ±0.4 s.e.).

However, we want to emphasize that there are limitations to our inverse modeling approach. One of these limitations is that it assumes all soil pore waters in the dataset evaporated along a fixed SEL slope, which may be too simplistic. In reality, the conditions affecting each evaporated sample are likely to vary temporally (e.g., temperature and humidity), resulting in variable SEL slopes. Another limitation to our approach is that it mainly relies on uniform changes in temperature (Equations S4 and S6). In reality, other factors such as relative humidity above the evaporating surface and seasonal changes in precipitation amount and isotopic composition (e.g., Figures S2 and S3) are also likely to play a role in the degree of evaporative fractionation[7, 44, 62].

Table S1. Forward model. Sources of input datasets, input files, and MATLAB model parameters.

Model input	Notation in code	Description	Data source
Luquillo_forward.csv	-	n x 4 table: depth (in cm), soil temperature in °C, $\delta^{18}O_{sw}$ and $\delta^{2}H_{sw}$	1) depth, $\delta^{18}O_{sw}$ and $\delta^{2}H_{sw}$ from ref. 66 2) soil temperature (see next row)
Luquillo_precip.csv	-	n x 3 table: meanTp (in °C), $\delta^{18}O_{p}$ and $\delta^{2}H_{p}$	see next rows
Oregon_forward.csv	-	n x 4 table: depth (in cm), soil temperature in °C, $\delta^{18}O_{sw}$ and $\delta^{2}H_{sw}$	1) depth, $\delta^{18}O_{sw}$ and $\delta^{2}H_{sw}$ from ref. 67 2) soil temperature (see next row)
Oregon_precip.csv	-	n x 3 table: meanTp (in °C), $\delta^{18}O_{p}$ and $\delta^{2}H_{p}$	see next rows
Air temperature	meanTp	long-term mean monthly air temperature Luquillo site Sabana, 2002-2008 Oregon site GSWS10, 1999-2019	Scatena, F., IITF (2020). LCZO -- Meteorology, Air Temperature -- Daily -- Luquillo Mountains -- (2002-2009)[114], HydroShare Gregory, S.; Johnson, S. 2019. Stream and air temperature data from stream gages and stream confluences in the Andrews Experimental Forest[115], 1950 to present
Soil temperature Luquillo wet and dry season air temp: 26.8 and 25.1 °C, respectively Oregon: mean annual air temp of 8.7 °C	soilT	modeled depth-associated soil temperature following Hillel (1982); see Equation 6	Model values based on input air temperature (meanTp) data
$\delta^{18}O_{sw}$ and $\delta^{2}H_{sw}$	d18O_soil d2H_soil	measured soil pore water isotopic compositions	Luquillo: Evaristo et al. (2016) Oregon: Brooks et al. (2010)
$\delta^{18}O_{p}$ and $\delta^{2}H_{p}$	d18Op d2Hp	amount-weighted monthly d18O and d2H of precipitation Luquillo Mountains (sites LQR3, LQR4,	Luquillo: U.S. Geological Survey Open-File Report 2014–1101[116], http://dx.doi.org/10.3133/ofr20141101

Model input	Notation in code	Description	Data source
		LQR5, LQR6) Oregon site PRIMET, 2014-2018	Oregon: Segura, C. 2022. Water stable isotopes for streams and precipitation samples in the HJ Andrews Experimental Forest and Mary's River Watershed, 2014-2018. Long-Term Ecological Research. Forest Science Data Bank, Corvallis, OR[117].

Table S2. Inverse model. Sources of input datasets, input files, and MATLAB model parameters.

Model input	Notation in code	Description	Data source
Finland_inverse.csv	-	n x 2 table: $\delta^{18}O_{kaol}$ and $\delta^{2}H_{kaol}$	From ref 19
Finland_precip.csv	-	n x 3 table: meanTp (in °C), $\delta^{18}O_{p}$ and $\delta^{2}H_{p}$	see next rows
Sierras_inverse.csv	-	n x 2 table: $\delta^{18}O_{kaol}$ and $\delta^{2}H_{kaol}$	From ref. 29, 83
Sierras_precip.csv	-	n x 3 table: meanTp (in °C), $\delta^{18}O_{p}$ and $\delta^{2}H_{p}$	see next rows
Air temperature	meanTp	long-term mean monthly air temperature Finland site Rovaniemi IAEA station Sierras site Auburn, Ca 1951-2010	Finland: GNIP, Finland Rovaniemi station[118] Sierras[119]: UCANR IPM
Soil temperature	soilT	modeled depth-associated soil temperature following Hillel (1982); see Equation 6	Model values based on input air temperature (meanTp) data
$\delta^{18}O_{kaol}$ and $\delta^{2}H_{kaol}$	d18O_kaol d2H_kaol	measured kaolinite isotopic compositions	Finland: ref. 19 Sierras: ref. 29, 83
$\delta^{18}O_{p}$ and $\delta^{2}H_{p}$	d18Op d2Hp	amount-weighted monthly d18O and d2H of precipitation Finland: Rovaniemi station[120] Sierras: Placer County[121]	Finland: GNIP, Finland IAEA Rovaniemi statio[120] Sierras: OIPC calculator[121] using geographic coordinates of Placer County, elevation 1292 ft (394 m)

References cited in supplemental text only

102. Goldsmith, G. R., Muñoz-Villers, L. E., Holwerda, F., McDonnell, J. J., Asbjornsen, H., & Dawson, T. E. (2012). Stable isotopes reveal linkages among ecohydrological processes in a seasonally dry tropical montane cloud forest. Ecohydrology, 5(6), 779-790.

103. West, Adam G., Shela J. Patrickson, and James R. Ehleringer. "Water extraction times for plant and soil materials used in stable isotope analysis." Rapid Communications in Mass Spectrometry: An International Journal Devoted to the Rapid Dissemination of Up-to-the-Minute Research in Mass Spectrometry 20.8 (2006): 1317-1321.

104. Orlowski, N., Breuer, L., & McDonnell, J. J. Critical issues with cryogenic extraction of soil water for stable isotope analysis. Ecohydrology, 9(1), 1-5 (2016).

105. Oerter, E., Finstad, K., Schaefer, J., Goldsmith, G. R., Dawson, T., & Amundson, R. (2014). Oxygen isotope fractionation effects in soil water via interaction with cations (Mg, Ca, K, Na) adsorbed to phyllosilicate clay minerals. Journal of Hydrology, 515, 1-9 (2014).

106. Meißner, M., Köhler, M., Schwendenmann, L., Hölscher, D., & Dyckmans, J. Soil water uptake by trees using water stable isotopes (δ 2 H and δ 18 O)− a method test regarding soil moisture, texture and carbonate. Plant and soil, 376, 327-335 (2014).

107. Newberry, S. L., Nelson, D. B., & Kahmen, A. Cryogenic vacuum artifacts do not affect plant water-uptake studies using stable isotope analysis. Ecohydrology, 10(8), e1892 (2017).

108. Newberry, S. L., Prechsl, U. E., Pace, M., & Kahmen, A. Tightly bound soil water introduces isotopic memory effects on mobile and extractable soil water pools. Isotopes in Environmental and Health Studies, 53(4), 368-381 (2017).

109. Evaristo, J., Jasechko, S., & McDonnell, J. J.. Global separation of plant transpiration from groundwater and streamflow. Nature, 525(7567), 91-94 (2015).

110. Hervé-Fernández, P., Oyarzún, C., Brumbt, C., Huygens, D., Bodé, S., Verhoest, N. E. C., & Boeckx, P. J. H. P. Assessing the ‘two water worlds’ hypothesis and water sources for native and exotic evergreen species in south-central Chile. Hydrological Processes, 30(23), 4227-4241 (2016).

111. Javaux, M., Rothfuss, Y., Vanderborght, J., Vereecken, H., & Brüggemann, N. Isotopic composition of plant water sources. Nature, 536(7617), E1-E3 (2016).

112. Dogramaci, S., Skrzypek, G., Dodson, W., & Grierson, P. F. Stable isotope and hydrochemical evolution of groundwater in the semi-arid Hamersley Basin of subtropical northwest Australia. Journal of Hydrology, 475, 281-293 (2012).

113. Telmer, K., & Veizer, J. Isotopic constraints on the transpiration, evaporation, energy, and gross primary production budgets of a large boreal watershed: Ottawa River basin, Canada. Global Biogeochemical Cycles, 14(1), 149-165 (2000).

114. Scatena, F., LCZO Meteorology, Air Temperature-Daily-Luquillo Mountains-(2002-2009), HydroShare https://www.hydroshare.org/resource/b39a41c1db56412cb3ccd3a0c042f1ec/ (2020).

115. Gregory, S.; Johnson, S. Stream and air temperature data from stream gages and stream confluences in the Andrews Experimental Forest, 1950 to present. https://doi.org/10.6073/pasta/9437d1603044f5b92189110dd8343763 (2019).

116. U.S. Geological Survey Open-File Report 2014–1101, http://dx.doi.org/10.3133/ofr20141101

117. Segura, C. Water stable isotopes for streams and precipitation samples in the HJ Andrews Experimental Forest and Mary's River Watershed, 2014-2018. Long-Term Ecological Research. Forest Science Data Bank, Corvallis, OR. https://doi.org/10.6073/pasta/00a943113f6915fab65db3979205f5f9 (2022).

118. Rovaniemi Climate. Climate Data. https://en.climate-data.org/europe/finland/rovaniemi/rovaniemi-677/ (2023).

119. UCANR-IPM. https://ipm.ucanr.edu/calludt.cgi/WXSTATIONDATA?STN=AUBURN.C (2023)

120. IAEA. https://websso.iaea.org/ Finland: GNIP, Finland Rovaniemi station (2023).

121. OIPC Waterisotopes.org. https://wateriso.utah.edu/waterisotopes/pages/data_access/oipc.html (2023).